Geosci. Model Dev. Discuss., doi:10.5194/gmd-2016-289, 2016
Manuscript under review for journal Geosci. Model Dev.
Published: 12 December 2016

Geoscientific Model Development Discussions

Development of the WRF-CO2 4DVar assimilation system

Tao Zheng[1], Nancy French[2], and Martin Baxter[3]

[1]Department of Geography, Central Michigan University, Mount Pleasant, MI. USA
[2]Michigan Technological Research Institute, Michigan Technological University, Ann Arbor, MI. USA
[3]Department of Earth and Atmospheric Sciences, Central Michigan University, Mount Pleasant, MI. USA

Correspondence to: Tao Zheng (zheng1t@cmich.edu)

Abstract. Regional atmospheric CO_2 inversions commonly use Lagrangian particle trajectory model simulations to calculate the required influence function. To provide an alternative, we developed an adjoint based four-dimensional variational (4DVar) assimilation system, WRF-CO2 4DVar. This system is developed based on the Weather Research and Forecasting (WRF) model system, including WRF-Chem, WRFPLUS, and WRFDA. In WRF-CO2 4DVR, CO_2 is modeled as a tracer and its feedback to meteorology is ignored. This configuration allows most WRF physical parameterizations to be used in the assimilation system without incurring a large amount of code development. WRF-CO2 4DVar solves for the optimized CO_2 emission scaling factors in a Bayesian framework. Two variational optimization schemes are implemented for the system: the first uses the L-BFGS-B and the second uses the Lanczos conjugate gradient (CG) in an incremental approach. We modified WRFPLUS forward, tangent linear, and adjoint models to include CO_2 related processes. The system is tested by simulations over a domain covering the continental United States at 48 km $\times$ 48 km grid spacing. The accuracy of the tangent linear and adjoint models are assessed by comparing against finite difference sensitivity. The system's effectiveness for CO_2 inverse modeling is tested using pseudo-observation data. The results of the sensitivity and inverse modeling tests demonstrate the potential usefulness of WRF-CO2 4DVar for regional CO_2 inversions.

1 Introduction

Quantification of surface-atmospheric carbon exchange is important for understanding the global carbon cycle (Peters et al., 2007). Both inventory based bottom-up and atmospheric inversion based top-down approaches have been widely used to investigate carbon sources and sinks. Most atmospheric CO_2 inversion methods are based on Bayes theorem, in which CO_2 flux is optimized by minimizing a quadratic form cost function consisting of background cost and observation cost. The minimization of the cost function can be achieved by analytical or variational approaches. Chevallier et al. (2005) provides a concise explanation of the differences between the two approaches. Streets et al. (2013) provides a comprehensive review of atmospheric chemistry inversions using satellite observations, many of which have been applied to CO_2 inversion.

Both analytical and variational inversions use a chemistry transport model (CTM) to relate CO_2 flux to atmospheric CO_2. From the perspective of an optimization system, atmospheric CO_2 forms the observation vector, and CO_2 flux forms the state vector to be optimized. Central to all CO_2 inversion approaches is the Jacobian matrix which relates changes in flux to change

Geosci. Model Dev. Discuss., doi:10.5194/gmd-2016-289, 2016
Manuscript under review for journal Geosci. Model Dev.
Published: 12 December 2016

in model-simulated atmospheric CO_2. For an inversion system with a $n \times 1$ state vector and a $m \times 1$ observation vector, its Jacobian matrix is a $m \times n$ matrix. Analytical inversions require the explicit construction of the Jacobian matrix, which can be carried out by either CTM (as the forward model) or its adjoint model. While a forward model calculates the Jacobian matrix by columns, an adjoint model calculates it by rows. The size of the state vector or observation vector determines the number of forward or adjoint model runs needed for constructing the Jacobian matrix. The practical limit imposed by the computational cost of the Jacobian matrix construction and the memory demand of matrix inversion often necessitate the aggregation of flux to reduce state vector size in analytical inversions, which leads to aggregation error (Bocquet, 2009; Kaminski et al., 2001; Turner and Jacob, 2015). In comparison, variational approaches do not require the Jacobian matrix to be explicitly constructed, instead they propagate the overall adjoint forcing backward in time in searching for the optimized state vector. On the other hand, analytical inversions yield an estimation of the posterior error along with the optimized flux. Variational inversions require significant extra computation to estimate the posterior error.

A number of four dimensional variational (4DVar) assimilation systems have been developed and applied to global scale CO_2 inversions. The off-line transport model Parameterized Chemistry Tracer Model (PCTM) (Kawa et al., 2004) and its adjoint have been used for CO_2 inversions (Baker et al., 2010, 2006; Butler et al., 2010; Gurney et al., 2005). Chevallier et al. (2005) developed a 4DVar system based on the LDMZ model (Hourdin et al., 2006) to assimilate CO_2 observation data from Television Infrared Observation the Satellite Operational Vertical Sounder (TOVS). This system has also been used to inverse surface CO_2 observation data (Chevallier et al., 2010). The TM5 4DVar system (Meirink et al., 2008), based on the TM5 global two-way nested transport model (Krol et al., 2005), is used in the CarbonTracker CO_2 data assimilation system (Peters et al., 2007) and is included in the TransCom satellite intercomparison experiment (Saito et al., 2011). TM5 4DVar has also been used to investigate total column CO_2 seasonal amplitude (Basu et al., 2011) and to assimilate the Greenhouse Gases Observing Satellite (GOSAT) observations (Basu et al., 2013). Another widely used inversion system is the GEOS-Chem 4DVar (Henze et al., 2007; Kopacz et al., 2009) with its CO_2 module updated by Nassar et al. (2010). GEOS-Chem 4DVar has been used to estimate CO_2 fluxes from the Tropospheric Emission Spectrometer (TES) and the GOSAT CO_2 observations (Nassar et al., 2011; Deng et al., 2014).

CO_2 inversions at regional scale have become an active research front in recent years, driven by the need to resolve biosphere-atmosphere carbon exchange at smaller scales (Gerbig et al., 2009), and by the need to address policy-relevant objectives, such as assessing emission reduction effectiveness (Ciais et al., 2014) and the impact of regional scale sources like wildland fire (French et al., 2011). Compared with global inversions, there are fewer model choices for regional inversions. GEOS-Chem 4DVar's nested simulation ability provides a means for regional inversions, such as its application for CH_4 inversion over North America (Wecht et al., 2014). The majority of regional inversions use analytical approaches and typically use a Lagrangian particle backward trajectory model to compute the required influence function. For instance, Gerbig et al. (2003) used an analytical approach to minimize for the cost function and STILT (Lin et al., 2003) model driven by assimilated meteorology to calculate the influence function. In a later study, STILT driven by ECMWF meteorology is used to calculate the influence

Geosci. Model Dev. Discuss., doi:10.5194/gmd-2016-289, 2016
Manuscript under review for journal Geosci. Model Dev.
Published: 12 December 2016

Geoscientific Model Development Discussions

function to investigate the impacts of vertical mixing error (Gerbig et al., 2008). More recently, Lauvaux et al. (2012) also used an analytical solution for cost function minimization and LPDM (Uliasz, 1993) to compute the influence function. In another study, Pillai et al. (2012) used STILT driven by meteorology data from WRF to calculate the influence function for comparing Lagrangian and Eulerian models for regional CO_2 inversions. To improve accuracy, STILT has been coupled to WRF, in which the latter provides online meteorology to STILT to avoid interpolation error (Nehrkorn et al., 2010).

Most of these global and regional inversion systems transport CO_2 using offline meteorology. An exception is the Monitoring Atmospheric Composition and Climate Interim Implementation (MACC-II) greenhouse gases system based on ECMWF Integrated Forecasting System (IFS) (Massart et al., 2016). In this system, CO_2 transport is computed online using the IFS model. Because meteorological fields are crucial determining the quality of transport (Agusti-Panareda et al., 2016; Locatelli et al., 2013), and model transport uncertainty is key to the inversion quality (Houweling et al., 2010), online transport based inversion systems have the potential to investigate and mitigate the transport error.

In this paper, we developed WRF-CO2 4DVar, a regional CO_2 inversion system with online meteorology. This system is developed by modifying the WRFDA and WRFPLUS system (v3.6) in a similar approach to that used by Guerrette and Henze (2015, 2016) (GH15/16 afterward) for black carbon emission inversion. WRFDA is a meteorology data assimilation system, which includes a 4DVar assimilation system and related adjoint and tangent linear models (WRFPLUS) (Barker et al., 2012; Huang et al., 2009). Designed to improve weather forecasts, WRFDA 4DVar optimizes meteorological initial and boundary conditions by assimilating a variety of observational data. We modified WRFPLUS to include CO_2 related processes and we configure the cost function so that the state vector consists of CO_2 flux instead of meteorological fields. In developing WRFDA-Chem for black carbon inversion, GH15/16 excluded radiation, cumulus, and microphysics parameterization schemes from the tangent linear model and adjoint model because developing these procedures for black carbon would incur a large amount of new code development. In WRF-CO2 4DVar, CO_2 is a tracer, meaning its impacts on meteorology are ignored. This configuration allows us to include full physics schemes in WRF-CO2 4DVar's tangent linear model and adjoint model with limited new code development (see Section 2.4.2). As transport model error is detrimental to 4DVar inversion accuracy (Fowler and Lawless, 2016; Gerbig et al., 2009), we deem it important to use the full physics schemes in the tangent linear and adjoint models for WRF-CO2 4DVar. In addition, while GH15/16 excluded convective transport of chemistry species in WRFDA-Chem, we developed the tangent linear and adjoint code for this process in WRF-CO2 4DVar to reduce the vertical mixing error (see Section 2.4.4). Like GH15/16, we implemented an incremental optimization with the Lanczos version of conjugate gradient, but we also implemented the L-BFGS-B based optimization and compared the performance of the two approaches (see Section 2.2 and 3.4)

The remainder of this paper is organized as follows: Section 2 details the implementation of the two variational optimization schemes for cost function minimization, and the modification to the tangent linear and adjoint models. Section 3 examines the

Geosci. Model Dev. Discuss., doi:10.5194/gmd-2016-289, 2016
Manuscript under review for journal Geosci. Model Dev.
Published: 12 December 2016

Geoscientific Model Development Discussions

accuracy of sensitivity calculated by the tangent linear and adjoint models, and the system's effectiveness in inverse modeling. Finally, a summary and outlook are presented in Section 4.

2 Method

This section describes the WRF-CO2 4DVar cost function configuration and the associated minimization schemes, followed by a description of the forward, tangent linear, and adjoint models.

2.1 Cost function configuration

WRF-CO2 4DVar is designed to optimize CO_2 flux by assimilating CO_2 observational data into an atmospheric chemistry transport model. CO_2 flux is optimized through use of a linear scaling factor:

$$E = k_{co2} \times \widetilde{E} \tag{1}$$

Where $\widetilde{E}$ is the CO_2 emission read from emission files, k_{co2} is the emission scaling factor, and E is the effective CO_2 flux. It is the effective flux that is used in WRF-Chem's emission driver to update CO_2 mixing ratio (q_{co2}). The emission scaling factor k_{co2}, its tangent linear variable g_k_{co2}, and its adjoint variable a_k_{co2} are used in calculating model sensitivity and minimizing the cost function defined in Eq. (2). The readers can find a list of the notations used in this article in Table 1.

The cost function $J(x)$ of WRF-CO2 4DVar follows the Bayes framework widely used in atmospheric chemistry and numerical weather prediction (NWP) data assimilations:

$$J(x) = J_b(x) + J_o(x) \tag{2}$$

Where the background cost function $J_b(x)$ is defined as

$$J_b(x) = \frac{1}{2}(x^n - x^b)\mathbf{B}^{-1}(x^n - x^b) \tag{3}$$

and the observation cost function $J_o(x)$ is defined as

$$J_o(x) = \frac{1}{2}\sum_{k=1}^{K}(H(M(x^n)) - y_k)\mathbf{R}^{-1}(H(M(x^n)) - y_k) \tag{4}$$

Like other data assimilation systems, WRF-CO2 4DVar is essentially an optimization scheme. Its state vector x consists of the emission scaling factors k_{co2}. The subscript k in Eq. (4) indicates the entire assimilation time period is evenly split into K observation windows during which observational data are ingested into the assimilation system.

In WRF-CO2 4DVar, we implemented two optimization schemes to minimize the cost function. The first scheme uses a limited memory BFGS minimization algorithm (L-BFGS-B) (Byrd et al., 1995) and the second uses the Lanczos version of

Geosci. Model Dev. Discuss., doi:10.5194/gmd-2016-289, 2016
Manuscript under review for journal Geosci. Model Dev.
Published: 12 December 2016

conjugate gradient (Lanczos CG) (Lanczos, 1950) minimization algorithm. Both schemes are iterative processes, and they call on WRF-CO2 4DVar model components (the forward, tangent linear, and adjoint models) to calculate the model sensitivity $\partial q_{co2}/\partial k_{co2}$ between the iterations. The two optimization schemes are described in Section 2.2 and 2.3, respectively, and the three model components are described in Section 2.4.

2.2 L-BFGS-B optimization

L-BFGS-B (Byrd et al., 1995) is a quasi-Newton method for nonlinear optimization with bound constraints. It utilizes the cost function gradient to approximate the Hessian matrix, which provides an estimation of posterior error. L-BFGS-B has been used in a number of atmospheric chemistry inverse model systems, including the GEOS-Chem adjoint model system (Henze et al., 2007) and the TM5 4DVar system (Meirink et al., 2008). The diagram in Fig. 1 demonstrates the steps involved in the L-BFGS-B based optimization scheme. The scheme is an iterative process which searches for the optimized k_{co2} by minimizing the cost function defined in Eq. (2-4). Between its iterations, the minimization algorithm L-BFGS-B requires the values of the cost function and cost function gradient, which are supplied by the forward model and the adjoint model as indicated in Fig. 1.

The calculation of the cost function is carried out based on Eq. (2-4). Starting with the prior estimate of k_{co2}, the forward model run generates the CO_2 mixing ratio q_{co2}, which is transformed from the WRF model space to the observation space by the forward observation operator H. This results in the $H(M(x^n))$ term in Eq. (4), which is then paired with the observation vector y_k to calculate the innovation vector $d_k = H(M(x^n)) - y_k$. Next, the innovation vector and observation error covariance $\mathbf{R}$ are used to calculate the observation cost function $J_o(x)$ as expressed in Eq. (4). Finally, the background cost function $J_b(x)$ is calculated according Eq. (3), and combined with the observation cost function $J_o(x)$ to form the total cost function $J(x)$ according to Eq. (2).

In addition to the cost function, L-BFGS-B also requires the cost function gradient $\nabla J(x)$ in searching for the optimized k_{co2}. The cost function gradient is calculated using Eq. (5).

$$\nabla J(x) = \sum_{k=1}^{K} \widetilde{M}^T \widetilde{H}^T R^{-1}(H(M(x^n) - y_k) + B^{-1}(x^n - x^b) \tag{5}$$

The first term on the right hand side of Eq. (5) is the observation cost function gradient and the second is the background cost function gradient. The observation cost function gradient is calculated in two steps: (1) The innovation vector is scaled by $\mathbf{R}^{-1}$ and transformed to the WRF model space by the adjoint observation operator, resulting in $\widetilde{H}^T\mathbf{R}^{-1}(H(M(x^n)) - y_k)$, which is the adjoint forcing. (2) The adjoint forcing is ingested by the WRF-CO2 adjoint model during its backward (in time) integration, which yields the observation cost function gradient. Supplied with the values of the cost function and cost function gradient, the L-BFGS-B algorithm finds a new value of k_{co2}, which is used for the next iteration. The iterative optimization process continues until a given convergence criterion is met.

Geosci. Model Dev. Discuss., doi:10.5194/gmd-2016-289, 2016
Manuscript under review for journal Geosci. Model Dev.
Published: 12 December 2016

Geoscientific Model Development Discussions

2.3 Incremental optimization

The second optimization scheme we implemented for WRF-CO2 4DVar is the incremental approach commonly used in NWP data assimilation systems, including ECWMF 4DVar (Rabier et al., 2000) and WRFDA (Barker et al., 2012). A major difference between the L-BFGS-B based optimization and the incremental optimization is that the former optimizes for the state vector while the latter optimizes for the state vector analysis increment. The incremental assimilation scheme uses a linear approximation to transform the observation cost function from what is defined in Eq. (4) to Eq. (6):

$$J_o(x) = \frac{1}{2}\sum_{k=1}^{K}(H(M(x^{n-1})) - y_k + \widetilde{H}(\widetilde{M}(x^n - x^{n-1})))\mathbf{R}^{-1}(H(M(x^{n-1})) - y_k + \widetilde{H}(\widetilde{M}(x^n - x^{n-1}))) \quad (6)$$

Compared to Eq. (4), Eq. (6) approximates the innovation vector by a sum of two parts. The first part, $H(M(x^{n-1})) - y_k$, is the innoviation vector from the previous iteration. The second part, $\widetilde{H}(\widetilde{M}(x^n - x^{n-1}))$, is the state vector analysis increment $(x^n - x^{n-1})$ transformed by the tangent linear model $\widetilde{M}$ and tangent linear observation operator $\widetilde{H}$. With the linear approximation of the cost function, the cost function gradient is calculated by Eq. (7)

$$\nabla J(x) = \sum_{k=1}^{K}\widetilde{M}^T\widetilde{H}^T\mathbf{R}^{-1}(H(M(x^{n-1}) - y_k)) + \mathbf{B}^{-1}(x^{n-1} - x^b) + \sum_{k=1}^{K}\widetilde{M}^T\widetilde{H}^T\mathbf{R}^{-1}(\widetilde{H}(\widetilde{M}(x^n - x^{n-1}))) + \mathbf{B}^{-1}(x^n - x^{n-1}) \quad (7)$$

In WRF-CO2 4DVar, the incremental optimization is implemented as a double loop in which the outer loop calculates the first and second items on the right hand side of Eq. (7), while the inner loop calculates the third and fourth items. The outer loop first calls the forward model M and adjoint model $\widetilde{M}^T$ to calculate $\widetilde{M}^T\widetilde{H}^T R^{-1}(H(M(x^{n-1}) - y_k))$ and $B^{-1}(x^{n-1} - x^b)$, which remain unchanged during the subsequent inner loop calculation. The analysis increment $(x^n - x^{n-1})$ is optimized in the inner loop, which calls the tangent linear and adjoint models to calculate the third and fourth items of Eq. (7). For the inner loop calculation, we use the Lanczos CG (Lanczos, 1950), which requires less memory than L-BFGS-B and can be readily adapted to distributed memory parallel computation. In addition, Lanczos CG can optionally estimate the lead eigenvalues of the cost function Hessian matrix ($\nabla^2 J(x)$).

2.4 Forward, tangent linear, and adjoint models

WRFPLUS consists of three model components: the WRF model, its tangent linear model, and its adjoint model (Barker et al., 2012; Huang et al., 2009). The three models are used by WRFDA to optimize the initial meteorological condition in order to improve numerical weather prediction. Unlike WRFDA, WRF-CO2 4DVar is designed to optimize CO_2 flux, instead of the meteorological initial and boundary conditions. This difference means CO_2 related processes are needed in WRF-CO2 4DVar's model components. To include the CO_2 related processes, we first use WRF-Chem to replace WRF as the forward model. Then, we conducted a thorough variable dependence analysis to determine how to modify the tangent linear and adjoint model in order keep them consistent with WRF-Chem (the forward model).

Geosci. Model Dev. Discuss., doi:10.5194/gmd-2016-289, 2016
Manuscript under review for journal Geosci. Model Dev.
Published: 12 December 2016

2.4.1 Forward model

We replaced WRF with WRF-Chem as the forward model component of WRF-CO2 4DVar. As an atmospheric chemistry extension of WRF, WRF-Chem includes chemistry, deposition, photolysis, advection, diffusion, and convective transport of chemistry species (Grell et al., 2005). These processes are included in different modules of WRF-Chem: ARW (Advanced Research WRF) dynamical core, physics driver, and chemistry driver. We use the GHG (Greenhouse Gas) tracer option of WRF-Chem but have the CO and CH_4 removed, leaving only CO_2 related procedures. In the emission driver, we use the CASA-GFED v4 biosphere flux (Randerson et al., 2012) to replace the online biogenic CO_2 model Vegetation Photosynthesis and Respiration Model (VPRM) (Mahadevan et al., 2008). This change is made because WRF-CO2 4DVar optimizes for CO_2 flux instead of online emission model parameters.

2.4.2 Variable dependence analysis

The tangent linear and adjoint models of WRFPLUS need to be modified to include the CO2 related processes so that they will be consistent with the forward model. The results of the variable dependence analysis is summarized in Table 2, which groups WRF-Chem processes into three categories regarding CO_2 tracer transport. The first category includes the chemistry processes that do not apply to CO_2. This category contains gas and aqueous phase chemistry, dry and wet deposition, and photolysis. Because they are not applied to CO_2, these processes are simply excluded from the forward, tangent linear, and adjoint models in WRF-CO2 4DVar.

The second category is comprised of the physical parameterizations that do not provide CO_2 tendency, but provide meteorological tendency. This category includes radiation, surface, cumulus, and microphysics parameterizations. While the full physics schemes of surface, cumulus, planetary boundary layer (PBL), and microphysics are used in the forward model of WRFPLUS, simplified versions of these schemes are used in its tangent linear and adjoint models. In addtion, WRFPLUS uses full radiation schemes (longwave and shortwave) in its forward model, but it excludes radiation schemes from its tangent linear model and adjoint model. The differences in the physical parameterizations between the forward model and tangent linear/adjoint models in a 4DVar system is a source of linearization error. For instance, Tremolet (2004) found linearization error in ECMWF 4DVar larger than expected and recommended more accurate linear physics for higher resolution 4DVar systems. Because WRF-CO2 4DVar ignores the impacts of CO_2 mixing ratio variation on the meteorological fields, no tangent linear and adjoint variables for meteorological fields are needed in its tangent linear model and adjoint model. Since this second category of processes are not directly involved in CO_2 transport, there is no need for their tangent linear and adjoint procedures in WRF-CO2 4DVar. In WRFPLUS's tangent linear model, we removed the tangent linear code of the simplied versions of the cumulus, surface, and microphysics schemes, and replaced them with the forward code of their corresponding full schemes as used in the forward model. An adjoint model conducts a forward sweep and a backward sweep. In WRFPLUS's adjoint model, the forward sweep updates the state variables and local variables just as in the forward model, but it also stores these

Geosci. Model Dev. Discuss., doi:10.5194/gmd-2016-289, 2016
Manuscript under review for journal Geosci. Model Dev.
Published: 12 December 2016

variables' values for the subsequent backward sweep, which updates the adjoint variables of the state variables. We removed the simplified versions of the cumulus, surface, and microphysics schemes used in the forward sweep of WRFPLUS's adjoint model, and replaced them with the full schemes used in the forward model. Since these processes do not directly modify CO_2 mixing ratio, we simply removed their corresponding adjoint code from the backward sweep of the adjoint model, as indicted by the 'X' in Table 2.

The third category includes advection, diffusion, emission, and turbulence mixing in PBL, along with convective transport of CO_2. Because these processes directly modify CO_2 mixing ratio, their tangent linear code and adjoint code are needed for WRF-CO2 4DVar. The modifications we made for advection and diffusion are described in Section 2.4.3, and those for emission, turbulent mixing in PBL, and convective transport of CO_2 are detailed in Section 2.4.4.

2.4.3 Advection and diffusion of CO2

WRF includes the advection and diffusion of inert tracers along with other scalars in its ARW dynamical core. The tangent linear and adjoint code of these processes has been implemented in WRFPLUS. It should be noted that the variables for these inner tracers are part of WRF, instead of WRF-Chem. WRF-Chem use a seperate array for its chemistry species. Since we replaced WRF with WRF-Chem as the forward model in WRF-CO2 4DVar, CO_2 mixing ratio are included in the chemistry array. In the GHG option of WRF-Chem we use for WRF-CO2 4DVar, CO_2 from different sources (anthropogenic, biogenic, biomass burning, and oceanic) are represented by separate variables in the chemistry array. Following the treatment for the inner tracers in WRFPLUS, we modified subroutines solve_em_tl and solve_em_ad to add the tangent linear and adjoint code for the advection and diffusion of the chem array. The modifications we made include adding calls to the procedures that calculate advection and diffusion tendencies, updating the chemistry array with the tendencies and boundary conditions, and addressing the Message Passing Interface (MPI) communications. The new upgrade to WRFPLUS described in (Zhang et al., 2013) greatly expedited this part of development for WRF-CO2 4DVar. The 'Add' in Table 2 for advection and diffusion emphasizes that their tangent linear and adjoint code are added to WRF-CO2 4DVar based on the existing WRFPLUS code without substantial new code development.

2.4.4 Vertical mixing of CO_2 in PBL and convective transport

An accurate representation of vertical mixing is important for inversion accuracy, because misrepresentation causes transport error, which manifests itself in the innovation vector and causes error in posterior estimation (Fowler and Lawless, 2016). For instance, Stephens et al. (2007) pointed out that global chemistry transport model error in vertical mixing and boundary layer thickness could cause significant overestimation of northern terrestrial carbon uptake. A comparison of four global models found that model transport uncertainty exceeds the target requirement for A-SCOPE mission of 0.02 Pg C yr^{-1} per 10^6 km_2 (Houweling et al., 2010). In addition, Jiang et al. (2008) reported that convective flux is likely underestimated in boreal winter and spring based on simulated upper tropospheric CO_2 from 2000 to 2004 using three chemistry transport models.

Geosci. Model Dev. Discuss., doi:10.5194/gmd-2016-289, 2016
Manuscript under review for journal Geosci. Model Dev.
Published: 12 December 2016

In WRF-Chem, chemistry vertical mixing is treated in three separate parts: in the vertical diffusion (subgrid scale filter) in dynamical core, in the PBL scheme in the physics driver, and within convective transport in the chemistry driver. The subgrid scale filter in dynamical core treats both horizontal and vertical diffusions, but vertical diffusion is turned off if a PBL scheme is used. While all PBL schemes implemented in WRF-Chem treat the vertical turbulent mixing of temperature and moisture, only the ACM2 PBL scheme also treats chemistry species (Pleim, 2007). We choose to use the ACM2 scheme in WRF-CO2 4DVar so that CO_2 vertical mixing is treated by the PBL parameterization. Convective transport of chemistry species in WRF-Chem is not treated by the cumulus scheme in the physics driver, but by a separate convective transport module (module_ctrans_grell) in the chemistry driver (Grell et al., 2004).

Because the ACM2 PBL and chemistry convective transport are not included in WRFPLUS, we developed their tangent linear and adjoint code for WRF-CO2 4DVar. We first used the automatic differentiation tool TAPENADE (Hascoet and Pascual, 2013) to generate the tangent linear and adjoint code based on the forward code: module_bl_acm for the ACM2 PBL and module_ctrans_grell for the chemistry convective transport. We then manually modified the TAPENADE generated code to remove redundancy and unnecessary loops. It should be pointed out that these code developments are made significantly simpler because the meteorological state variables are merely passive variables in the tangent linear and adjoint code. For instance, to calculate the moist static energy and environmental values on cloud levels, the chemistry convective transport code (module_ctrans_grell) in the chemistry driver calls a number of subroutines in the cumulus parameterization code in the physics driver. Because these subroutines in cumulus parameterization only involve meteorology state variables and not the chemistry array, no tangent linear or adjoint code is needed for them in WRF-CO2 4DVar.

3 Results

This section presents an accuracy assessment of the newly developed WRF-CO2 4DVar system. We first describe the simulation model setup, then the sensitivity tests and inverse modeling experiments.

3.1 Model setup

WRF-CO2 4DVar is set up with a domain covering the continental United States with 48 km $\times$ 48 km grid spacing and 50 vertical levels. Model configuration includes: Rapid Radiative Transfer Model (RRTM) longwave radiation (Mlawer et al., 1997), Goddard shortwave radiation (Chou and Suarez, 1999), Pleim surface layer (Pleim, 2006), Pleim-Xiu land surface model (Pleim and Xiu, 2003), ACM2 PBL (Pleim, 2007), Grell-Freitas cumulus (Grell and Freitas, 2014), and Thompson microphysics (Thompson et al., 2008). Positive-definite transport is applied to the transport of scalars and CO_2. Emissions inventories used for the simulations include: anthropogenic flux from the Emission Database for Global Atmospheric Research (EDGAR; http://edgar.jrc.ec.europa.eu/index.php) version 4.2, biosphere flux from CASA-GFED v4 (Randerson et al., 2012), and ocean flux from Estimating the Circulation and Climate of the Ocean Phase II (ECCO2)-Darwin(Menemenlis et al., 2008).

Geosci. Model Dev. Discuss., doi:10.5194/gmd-2016-289, 2016
Manuscript under review for journal Geosci. Model Dev.
Published: 12 December 2016

A common emission scaling factor is applied to the combined EDGAR and CASA-GFED CO_2 flux, both of which are disaggregated to daily values before being ingested by WRF-CO2 4DVar. ECCO2-Darwin ocean flux is used in the simulations, but not included as the assimilation system's control variables. The model configuration and emission inventories used are summarized in Table 3.

Model simulation spans 24 hours from 00 UTC 02 June to 00 UTC 03 June, 2011. Meteorological initial and lateral boundary conditions are prepared using NCEP Climate Forecast System Version 2 (CFSv2) 6-hourly products (Saha et al., 2014). CO_2 initial condition and lateral boundary conditions are generated by running a WRF-Chem global domain simulation for the 120 hours prior to and during the WRF-CO2 4DVar simulations period. Figure 3 shows the model domain (bold outline) with its terrestrial region colored by the CASA-GFED biosphere CO_2 flux. The red triangles in the figure mark the locations of 20 tower sites at which model sensitivities are assessed in Section 3.3.

3.2 Spatial patterns of sensitivities

First, the forward model (WRF-Chem) was run for 24 hours with the CO_2 emission as described in the last section. Trajectory files that contain model state variables including both meteorology and CO_2 mixing ratio are saved at model dynamical time step intervals (120 seconds). These files are required for the subsequent tangent linear and adjoint model runs. Figure 4 shows the instantaneous values of Sea Level Pressure (SLP) and horizontal wind at the model's lowest vertical level at 06 UTC, 12 UTC, 18 UTC, and 23 UTC of 2 June 2011. The figure shows that a high pressure system was located off the west coast, causing a northerly surface wind off southern California, and a westerly wind for most of the Pacific Northwest. A low pressure system intensified over Montana and North Dakota during the 24 hours, causing a strong southerly wind over the Midwest. In the northeast, as a low pressure system moved eastward out of the domain, the surface wind shifted from southwesterly to westerly.

A tangent linear model run for a grid cell will calculate the tangent linear sensitivity $\partial q_{co2}/\partial k_{co2}$, which approximates a column vector of the forward model's Jacobian matrix and quantifies the influence of the cell's emission change on CO_2 mixing ratio of its receptor cells downwind. In comparison, an adjoint model run for a grid cell will calculate adjoint sensitivity $\partial q_{co2}/\partial k_{co2}$, which approximates a row vector of the forward model's Jacobian matrix and quantifies the influence on the cell's CO_2 mixing ratio by its source cells upwind. Because k_{co2} multiplies emission in Eq. (1), the magnitude of the sensitivity is determined by both the magnitude of emission and meteorological transport.

We first examined the influence of the meteorological transport on sensitivity by excluding the influence of emission magnitude. This is done by setting emission at all grid cells to unity (1 mol km^{-2} h^{-1}) for a given tangent linear or adjoint model run. To calculate tangent linear sensitivity at a grid cell, g_k_{co2} is set to unity at the cell and zero at all other cells at the start of a tangent linear model run. Upon completion, the values of g_q_{co2} are the tangent linear sensitivities $\partial q_{co2}/\partial k_{co2}$. Because emissions are set to unity at all model cells, the unit of such obtained sensitivity is ppm/(mol km^{-2} h^{-1}). To calculate adjoint sensitivity at a cell, an adjoint model run starts with a_q_{co2} set to unity at the cell and zero at all others, and the values of

Geosci. Model Dev. Discuss., doi:10.5194/gmd-2016-289, 2016
Manuscript under review for journal Geosci. Model Dev.
Published: 12 December 2016

a_k_{co2} at the end of the simulation are the adjoint sensitivities. The adjoint model running in this mode is analogous to using a Lagrangian particle transport model in backward trajectory mode to compute the footprint at a receptor, such as shown in Fig 4. of (Gerbig et al., 2003).

Table 4 lists the locations of tower sites marked on Fig 3. We calculated tangent linear and adjoint sensitivities at each of the grid cells where these tower sites are located. Figure 5 shows the results for Ozarks, Missouri (top row) and WLEF, Wisconsin (bottom row). Tangent linear sensitivity at Ozarks shows that the areas where surface level CO_2 are most influenced by Ozarks are located north and northwest of it. In comparison, adjoint sensitivity at Ozarks shows its surface level CO_2 was most influenced by the emission of areas located to the south of it. The spatial patterns of both the tangent linear and adjoint sensitivities at Ozarks indicate the influence of meteorological transport of CO_2 (Fig. 3), as surface wind in this area was largely southerly and southeasterly during the simulation period. In comparison, the tangent linear and adjoint sensitivities at WLEF (lower row of Fig. 4) show that its receptor cells are largely located to its west and its source cells located to its southeast. Surface wind over Wisconsin and Minnesota was easterly and southeasterly during the simulation period (Fig. 3), confirming the sensitivities' spatial patterns. The results from Sutro, California (top row) and Hidden Peak, Utah (bottom row) are shown in Fig 6. While the adjoint sensitivities (right column) in Fig. 6 show that both sites are mostly influenced by areas west of them owing to the steady westerly wind (Fig. 3), the tangent linear sensitivities (left column) show marked differences in their influence downwind: The northerly wind along the Californian coast advects Sutro's emission southward, the southwesterly wind over Utah, Colorado, and Wyoming advects Hidden Peak's emission toward northeast. The tangent linear and adjoint sensitivities patterns correlate similarly with the meteorology at the other 16 sites (no shown).

3.3 Accuracy of tangent linear and adjoint sensitivities

We next examined the accuracy of the tangent linear and adjoint models by comparing their sensitivity calculations against the finite difference sensitivity calculated using the two-sided formula (Eq. (8)).

$$\frac{\partial f}{\partial x} = \frac{f(x+\Delta x) - f(x-\Delta x)}{2\Delta x} \tag{8}$$

All results described in this section are obtained by model simulations with full emissions as described in Section 3.1. The resulting sensitivities $\partial q_{co2}/\partial k_{co2}$ include the influence of both meteorological transport and the magnitude of emission, and their units are ppm. This is different from the results represented in Section 3.2, where the sensitivities do not include the influence of the magnitude of emission.

Using Eq. (8), two forward model runs were used to calculate the finite sensitivity at a given grid cell, which forms a column vector of the model's Jacobian matrix. Because both finite difference and tangent linear sensitivities form columns of the Jacobian matrix, their values can be compared cell by cell for all receptor cells for a given site. Figure 7 shows the comparison between the finite difference and tangent linear sensitivities at nine sites. The dark straight lines in the figures are the 1:1 line. At two of the sites, WLEF and Cannan Valley, the sensitivity $\partial q_{co2}/\partial k_{co2}$ shows negative values, due to the fact that the

Geosci. Model Dev. Discuss., doi:10.5194/gmd-2016-289, 2016
Manuscript under review for journal Geosci. Model Dev.
Published: 12 December 2016

combined EDGAR and CASA-GFED emission is negative (carbon sink). The slope and R^2 of the linear fit show that the tangent linear sensitivity agrees very well with the finite difference sensitivity. Results at the other 11 sites are similar (not shown).

We next examined the accuracy of the adjoint model. Because finite difference sensitivities form columns of the Jacobian matrix while adjoint sensitivities form rows of the Jacobian matrix, they can only be compared at the intersections of the rows and columns for the 20 sites. For the 24-hour simulation, sensitivity at most of these intersections are zero except for those where a cell is both a receptor and source. We compared adjoint and finite difference sensitivities at the 20 sites and the result is shown in Fig. 8. The result from Sutro, California is shown in an inset due to its much larger magnitude as the site is close to the large anthropogenic emission from San Francisco. The two sets of sensitivities compare well, with the linear fit slope equal to 0.9994 and R^2 equal to 0.9997.

3.4 Inverse modeling test

After confirming the validity of the tangent linear and adjoint models, we tested the effectiveness of WRF-CO2 4DVAR in inverse modeling experiments. Pseudo-observation data generated by the forward model run are used in these inverse modeling experiments, which start with prescribed prior values of the emission scaling factors and seek to recover their true values. To generate pseudo-observation data, the forward model ran for 24 hours with EDGAR and CASA-GFED emission (disaggregated to daily values), saving CO_2 mixing ratio (q_{co2}) every 4 hours. This generated a set of six pseudo-observation files, each of which include the instantaneous q_{co2} at the model's lowest layer at all grid cells.

We conducted inverse modeling experiments for two cases of prior k_{co2}. In the first case, the prior emission scaling factor underestimates the true values by 50% ($k_{co2} = 0.5$ at all cells). In the second case, the prior emission scaling factor overestimates the true values by 50% ($k_{co2} = 1.5$ at all cells). Both L-BFGS-B and incremental optimization (Lanczos CG) are applied to the two cases, giving four inverse modeling experiments in total. In all four experiments, background error covariance is set to infinity ($\mathbf{B^{-1}} = \mathbf{0}$) and equal weights are assigned to all observations ($\mathbf{R}$ set to identify matrix). Because the pseudo-observation data are of q_{co2} from the forward model's lowest layer, the mapping between model space and observation space is trivial: the observation operator, tangent linear observation operator, and adjoint observation operator are all set to the identity matrix.

The results from inverse modeling experiments with prior emission scaling facotr k_{co2}=0.5 are shown in Fig 9 and 10. Figure 9 shows the iterative reduction of the cost function $J(x)$ (top) and cost function gradient norm $\|\nabla J(x)\|$ (bottom). By the 30^{th} iteration, the cost function is reduced to 0.42×10^{-5} and 1.54×10^{-5} of its starting value by the Lanczos-CG and L-BFGS-B and Lanczos-CG optimization, respectively. The figure shows that Lanczos-CG reduces the cost function faster than L-BFGS-B in the first 10 iterations, but its reduction rate slows down and stagnates at round the 15^{th} iteration, caused by the gradual loss of conjugacy. Lanczos-CG exits from its inner loop at end of 16^{th} iteration and starts a second outer loop in which the forward model is called to run with the last optimized k_{co2}, and the adjoint model is called to update the adjoint forcing. This

Geosci. Model Dev. Discuss., doi:10.5194/gmd-2016-289, 2016
Manuscript under review for journal Geosci. Model Dev.
Published: 12 December 2016

Geoscientific Model Development Discussions

results in a renewed conjugacy and increased cost function reduction rate. In comparison, L-BFGS-B has a more consistent cost function reduction rate through the iterations. The lower panel of Fig. 9 shows that by the 30^{th} iteration cost function gradient norm $\|\nabla J(x)\|$ is reduced to 0.6×10^{-3} and 1.35×10^{-3} of its starting value by the L-BFGS-B and Lanczos-CG optimization, respectively. Whereas the Lanczos-CG results in a largely monotonic decreasing $\|\nabla J(x)\|$, L-BFGS-B features oscillations but results in a overall downward trend.

Figure 10 shows the progress of the optimized CO_2 emission, obtained by multiplying the combined EDGAR/CASA-GFED emission with the optimized k_{co2}. The figure shows the comparison between the true emission value and optimized values after the 1^{st}, 5^{th}, 10^{th}, 20^{th}, and 30^{th} iterations by both optimization approaches. The straight line in each figure is the 1:1 line, and Root Mean Squared Error (RMSE) is given in each figure. The figures show that after the first iteration, the L-BFGS-B optimized emission barely departed from the prior value, reflecting the very small reduction in cost function by L-BFGS-B in its first several iterations as shown in Fig. 9. In comparison, the first iteration by Lanczos-CG substantially moved the optimized emission toward the true values. The figure also shows that both optimization schemes sometimes push underestimated values to overestimates. After the 5^{th} iteration, the patterns are very similar between the two optimization schemes, although RMSE still indicates substantial differences. The L-BFGS-B optimization achieves a smaller RMSE than Lanczos-CG by the 20^{th} iteration, mirroring the cost function and cost function gradient norm reduction trend shown in Fig. 9. Starting at 2336.5 mol km^{-2} h^{-1}, RMSE is reduced to 17.0 and 42.6 mol km^{-2} h^{-1} after 30 iterations by the L-BFGS-B and Lanczos-CG, respectively.

The results of inverse modeling experiments with prior emission scaling factor $k_{co2} = 1.5$ are shown in Fig. 11 and 12. The reductions of $J(x)$ and $\|\nabla J(x)\|$ are similar to the first case. Figure 11 shows that in 29 iterations, L-BFGS-B reduces cost function to 0.38×10^{-5} of its starting value, out-performing Lanczos CG (0.87×10^{-5}). The cost function gradient norm $\|\nabla J(x)\|$ is reduced to 0.45×10^{-3} and 0.91×10^{-3} of its starting value by L-BFGS-B and Lanczos-CG, respectively. Figure 12 shows the iterative optimization of CO_2 emission by the two optimization approaches. Similar to the first case, L-BFGS-B results in a slower reduction of RMSE in about the first 10 iterations, but catches up with the Lanczos-CG afterward. After 29 iterations, the RMSE has been reduced from 2336.5 mol km^{-2} h^{-1} to 20.2 and 22.19 mol km^{-2} $h^{-1}$by the L-BFGS-B and Lanczos-CG, respectively. Table 5 summarizes the results from the all four inverse modeling experiments described above.

4 Summary and outlook

While the rising atmospheric CO_2 has been well documented by observational data, major uncertainties still exist in attributing it to specific processes. For instance, the two sets of terrestrial biosphere CO_2 flux databases in NASA's carbon monitoring system flux pilot project differ substantially (Ott et al., 2015). In order to better resolve the terrestrial biosphere's response to the rising CO_2, inverse modeling at the regional scale is a high research priority (Gerbig et al., 2009).

Geosci. Model Dev. Discuss., doi:10.5194/gmd-2016-289, 2016
Manuscript under review for journal Geosci. Model Dev.
Published: 12 December 2016

Toward this end, we developed the WRF-CO2 4DVar, a data assimilation system designed to constrain surface CO_2 flux by combining an online atmospheric chemistry transport model and observation data in a Bayesian framework. We implemented two optimization schemes for cost function minimization. The first is based on L-BFGS-B and the second is an incremental optimization using Lanczos-CG. The cost function and its gradient required by the optimization schemes are calculated by WRF-CO2 4DVar's three component models: forward, tangent linear, and adjoint model, all developed on top of the WRF-PLUS system. While WRFPLUS's forward model is WRF, we use WRF-Chem as WRF-CO2 4DVar's forward model to include CO_2 in the system, and we modified the tangent linear and adjoint models to keep their consistency with the forward model. Like most other CO_2 inverse modeling system, WRF-4DVar ignores the possible impacts of atmospheric CO_2 variation on the meteorology. This simplification enables us to use the same full physical parameterizations in the forward, tangent linear, and adjoint model. Such configuration reduces linearization error while allowing the WRF system's large number of physical parameterizations to be used in WRF-CO2 4DVar without incurring a large amount of new code development.

We tested WRF-CO2 4DVar's tangent linear and adjoint models by comparing their sensitivities' spatial patterns with the dominant wind patterns. The results make physical sense given the meteorological transport. We evaluated the accuracy of tangent linear and adjoint models by comparing their sensitivity against finite difference sensitivity calculated by the forward model. The results show that both tangent linear and adjoint sensitivities agree well with finite difference sensitivity. At last, we tested the system in inverse modeling with pseudo-observation data, and the results show that both optimization schemes successfully recovered the true values with reasonable accuracy and computation cost.

The two optimization schemes have their respective advantages and disadvantages. Lanczos CG based incremental optimization requires less memory and is more amenable to parallel programming, both of which are desirable for large dimension optimization problems typical in atmospheric chemistry inverse modeling. As a quasi-Newton approach, L-BFGS-B may converge faster than Lanczos CG, and it can be extended to provide an approximation of the cost function's inverse Hessian, which is also the posterior error covariance. However, L-BFGS-B requires much more memory, especially if one chooses to update the inverse Hessian.

A potential application for WRF-CO2 4DVar will be using satellite CO_2 data to estimate surface flux. Technological advancement in satellite remote sensing has led to increasingly refined footprint size of CO_2 sensors. While the smaller footprint has the advantage of allowing CO_2 measurement during scattered cloud conditions, the mismatch between the satellite retrieval footprint size and the larger atmospheric chemistry transport model grid causes representation error (Pillai et al., 2010). Because scale mismatch caused representation errors will lead to systematic bias in CO_2 flux estimates, it is desirable to use a transport model with finer grid spacing. In this regard, the WRF-CO2 4DVar system provides the flexibility of using any model grid spacing.

Geosci. Model Dev. Discuss., doi:10.5194/gmd-2016-289, 2016
Manuscript under review for journal Geosci. Model Dev.
Published: 12 December 2016

Although using a high resolution transport model could reduce scale mismatch and the related representation error, its actual application needs to address the balance of aggregation and smoothing error (Turner and Jacob, 2015). For instance, if WRF-CO2 4DVar's model grid spacing decreases from 48 km × 48 km to 12 km × 12 km to better match the footprint size of GOSAT measurement, its state vector dimension will increase 16 times. The much larger state vector is not likely to be sufficiently constrained by observations, leading to smoothing error (Kaminski et al., 2001; Wecht et al., 2014). On the other hand, decreasing model resolution means a smaller state vector and less smoothing error, but the spatial patterns of emission in the large grids are imposed by prior knowledge and not allowed to be optimized, leading to aggregation error (Kaminski et al., 2001; Schuh et al., 2009). A solution toward an optimal balance of the representation, aggregation, and smoothing errors is to use a high resolution transport model but aggregate the transport model's native grid to reduce the state vector dimension. A number of studies have been conducted to search for the optimal aggregation approaches (Wu et al., 2011; Turner and Jacob, 2015; Bocquet, 2009; Bocquet et al., 2011). A mapping mechanism between WRF-4DVar's native grid and state vector can be easily implemented to test such aggregation approaches.

Another potential application of WRF-CO2 4DVar is to investigate transport model uncertainty. For instance, Ott et al. (2009) analyzed atmospheric tracer sensitivity to convective transport parameterization, and Gerbig et al. (2009) investigated CO_2 inversion uncertainty caused by the transport model, including advection, PBL mixing, convection, and mesoscale processes. With its online meteorology and flexibility in configuring physical parameterizations and dynamical processes, WRF-CO2 4DVar provides a versatile platform for investigating transport model related error in CO_2 inversions.

Regarding its applications in the above discussed areas, we will address the following issues in the future development of WRF-CO2 4DVar: (1) developing observation operators for satellite retrieved column-averaged dry air mole fraction of CO2 (XCO_2); (2) implementing the option to include the initial and lateral boundary conditions of atmospheric CO_2 in the state vector.

5 Code availability

The source code and compilation instruction of the WRF-CO2 4DVar assimilation system can be obtained by contacting the lead author: T. Zheng (zheng1t@cmich.edu). A full release of the source code for the public use is being prepared. The system is under continuous development and major updates in the future will be released too.

Acknowledgements. The authors express their appreciation for the WRF/WRF-Chem/WRFDA/WRFPLUS development teams for making their code available in the public domain. Discussion with Joel BeLanc of Michigan Technological Research Institute (MTRI) improved the optimization schemes implementation and presentation in this paper.

Geosci. Model Dev. Discuss., doi:10.5194/gmd-2016-289, 2016
Manuscript under review for journal Geosci. Model Dev.
Published: 12 December 2016

References

Agusti-Panareda, A., Massart, S., Chevallier, F., Balsamo, G., Boussetta, S., Dutra, E., and Beljaars, A.: A biogenic CO2 flux adjustment scheme for the mitigation of large-scale biases in global atmospheric CO2 analyses and forecasts, Atmos. Chem. Phys., 16, 10 399–10 418, doi:10.5194/acp-16-10399-2016, 2016.

Baker, D. F., Doney, S. C., and Schimel, D. S.: Variational data assimilation for atmospheric CO2, Tellus Ser. B-Chemical and Physical Meteorology, 58, 359–365, 2006.

Baker, D. F., Boesch, H., Doney, S. C., O'Brien, D., and Schimel, D. S.: Carbon source/sink information provided by column CO2 measurements from the Orbiting Carbon Observatory, Atmos. Chem. Phys., 10, 4145–4165, 2010.

Barker, D., Huang, X.-Y., Liu, Z., Auligne, T., Zhang, X., Rugg, S., Ajjaji, R., Bourgeois, A., Bray, J., Chen, Y., Demirtas, M., Guo, Y.-R., Henderson, T., Huang, W., Lin, H.-C., Michalakes, J., Rizvi, S., and Zhang, X.: The Weather Research and Forecasting Model's Community Variational/Ensemble Data Assimilation System Wrfda, Bull. Amer. Meteor. Soc., 93, 831–843, 2012.

Basu, S., Houweling, S., Peters, W., Sweeney, C., Machida, T., Maksyutov, S., Patra, P. K., Saito, R., Chevallier, F., Niwa, Y., Matsueda, H., and Sawa, Y.: The seasonal cycle amplitude of total column CO2: Factors behind the model-observation mismatch, J. Geophys. Res.-Atmospheres, 116, 2011.

Basu, S., Houweling, S., Peters, W., Sweeney, C., Machida, T., Maksyutov, S., Patra, P. K., Saito, R., Chevallier, F., Niwa, Y., Matsueda, H., and Sawa, Y.: The seasonal cycle amplitude of total column CO2: Factors behind the model-observation mismatch, J. Geophys. Res.-Atmospheres, 116, 2013.

Bocquet, M.: Toward Optimal Choices of Control Space Representation for Geophysical Data Assimilation, Mon. Weather Rev., 137, 2331–2348, 2009.

Bocquet, M., Wu, L., and Chevallier, F.: Bayesian design of control space for optimal assimilation of observations. Part I: Consistent multiscale formalism, Quart. J. Roy. Meteor. Soc., 137, 1340–1356, 2011.

Butler, M. P., Davis, K. J., Denning, A. S., and Kawa, S. R.: Using continental observations in global atmospheric inversions of CO2: North American carbon sources and sinks, Tellus Ser. B-Chemical and Physical Meteorology, 62, 550–572, sI, 2010.

Byrd, R. H., Lu, P., and Nocedal, J.: A limited memory algorithm for bound constrained optimization, SIAM Journal on Scientific and Statistical Computing, 16, 1190–1208, 1995.

Chevallier, F., Fisher, M., Peylin, P., Serrar, S., Bousquet, P., Breon, F. M., Chedin, A., and Ciais, P.: Inferring CO2 sources and sinks from satellite observations: Method and application to TOVS data, J. Geophys. Res.-Atmospheres, 110, d24309, 2005.

Chevallier, F., Ciais, P., Conway, T. J., Aalto, T., Anderson, B. E., Bousquet, P., Brunke, E. G., Ciattaglia, L., Esaki, Y., Froehlich, M., Gomez, A., Gomez-Pelaez, A. J., Haszpra, L., Krummel, P. B., Langenfelds, R. L., Leuenberger, M., Machida, T., Maignan, F., Matsueda, H., Morgui, J. A., Mukai, H., Nakazawa, T., Peylin, P., Ramonet, M., Rivier, L., Sawa, Y., Schmidt, M., Steele, L. P., Vay, S. A., Vermeulen, A. T., Wofsy, S., and Worthy, D.: CO2 surface fluxes at grid point scale estimated from a global 21 year reanalysis of atmospheric measurements, J. Geophys. Res.-Atmospheres, 115, d21307, 2010.

Chou, M. D. and Suarez, M.: A solar radiation parameterization for atmospheric studies, Tech. Rep. NASA/TM-1999-10460, vol. 15, 38 pp, NASA, 1999.

Ciais, P., Dolman, A. J., Bombelli, A., Duren, R., Peregon, A., Rayner, P. J., Miller, C., Gobron, N., Kinderman, G., Marland, G., Gruber, N., Chevallier, F., Andres, R. J., Balsamo, G., Bopp, L., Breon, F. M., Broquet, G., Dargaville, R., Battin, T. J., Borges, A., Bovensmann, H., Buchwitz, M., Butler, J., Canadell, J. G., Cook, R. B., DeFries, R., Engelen, R., Gurney, K. R., Heinze, C., Heimann, M., Held, A., Henry,

M., Law, B., Luyssaert, S., Miller, J., Moriyama, T., Moulin, C., Myneni, R. B., Nussli, C., Obersteiner, M., Ojima, D., Pan, Y., Paris, J. D., Piao, S. L., Poulter, B., Plummer, S., Quegan, S., Raymond, P., Reichstein, M., Rivier, L., Sabine, C., Schimel, D., Tarasova, O., Valentini, R., Wang, R., van der Werf, G., Wickland, D., Williams, M., and Zehner, C.: Current systematic carbon-cycle observations and the need for implementing a policy-relevant carbon observing system, BIOGEOSCIENCES, 11, 3547–3602, doi:10.5194/bg-11-3547-2014, 2014.

Deng, F., Jones, D. B. A., Henze, D. K., Bousserez, N., Bowman, K. W., Fisher, J. B., Nassar, R., O'Dell, C., Wunch, D., Wennberg, P. O., Kort, E. A., Wofsy, S. C., Blumenstock, T., Deutscher, N. M., Griffith, D. W. T., Hase, F., Heikkinen, P., Sherlock, V., Strong, K., Sussmann, R., and Warneke, T.: Inferring regional sources and sinks of atmospheric CO2 from GOSAT XCO2 data, Atmos. Chem. Phys., 14, 3703–3727, 2014.

Fowler, A. M. and Lawless, A. S.: An Idealized Study of Coupled Atmosphere–Ocean 4D-Var in the presence of model error, Mon. Weather Rev., 144, 4007–4029, doi:10.1175/MWR-D-15-0420.1, 2016.

French, N. H. F., de Groot, W. J., Jenkins, L. K., Rogers, B. M., Alvarado, E., Amiro, B., de Jong, B., Goetz, S., Hoy, E., Hyer, E., Keane, R., Law, B. E., McKenzie, D., McNulty, S. G., Ottmar, R., Perez-Salicrup, D. R., Randerson, J., Robertson, K. M., and Turetsky, M.: Model comparisons for estimating carbon emissions from North American wildland fire, J. Geophys. Res.-BIOGEOSCIENCES, 116, doi:10.1029/2010JG001469, 2011.

Gerbig, C., Lin, J. C., Wofsy, S. C., Daube, B. C., Andrews, A. E., Stephens, B. B., Bakwin, P. S., and Grainger, C. A.: Toward constraining regional-scale fluxes of CO2 with atmospheric observations over a continent: 1. Observed spatial variability from airborne platforms, J. Geophys. Res.-Atmospheres, 108, 4756, 2003.

Gerbig, C., Korner, S., and Lin, J. C.: Vertical mixing in atmospheric tracer transport models: error characterization and propagation, Atmos. Chem. Phys., 8, 591–602, 2008.

Gerbig, C., Dolman, A. J., and Heimann, M.: On observational and modelling strategies targeted at regional carbon exchange over continents, Biogeosciences, 6, 1949–1959, 2009.

Grell, G. A. and Freitas, S. R.: A scale and aerosol aware stochastic convective parameterization for weather and air quality modeling, Atmos. Chem. Phys., 14, 5233–5250, doi:10.5194/acp-14-5233-2014, 2014.

Grell, G. A., Knoche, R., Peckham, S. E., and McKeen, S. A.: Online versus offline air quality modeling on cloud-resolving scales, Geophys. Res. Lett., 31, l16117, 2004.

Grell, G. A., Peckham, S. E., Schmitz, R., McKeen, S. A., Frost, G., Skamarock, W. C., and Eder, B.: Fully coupled online chemistry within the WRF model, Atmos. Environ., 39, 6957–6975, 2005.

Guerrette, J. J. and Henze, D. K.: Development and application of the WRFPLUS-Chem online chemistry adjoint and WRFDA-Chem assimilation system, Geosci. Model Dev., 8, 1857–1876, 2015.

Guerrette, J. J. and Henze, D. K.: Four dimensional variation of black carbon emissions during ARACTAS-CARB with WRFDA-Chem, Atmos. Chem. Phys. Discuss., doi:10.5194/acp-2016-573, 2016.

Gurney, K. R., Chen, Y. H., Maki, T., Kawa, S. R., Andrews, A., and Zhu, Z. X.: Sensitivity of atmospheric CO2 inversions to seasonal and interannual variations in fossil fuel emissions, J. Geophys. Res.-Atmospheres, 110, d10308, 2005.

Hascoet, L. and Pascual, V.: The Tapenade Automatic Differentiation Tool: Principles, Model, and Specification, ACM Trans. Math. Software, 39, 20, 2013.

Henze, D. K., Hakami, A., and Seinfeld, J. H.: Development of the adjoint of GEOS-Chem, Atmos. Chem. Phys., 7, 2413–2433, 2007.

Geosci. Model Dev. Discuss., doi:10.5194/gmd-2016-289, 2016
Manuscript under review for journal Geosci. Model Dev.
Published: 12 December 2016

Hourdin, F., Musat, I., Bony, S., Braconnot, P., Codron, F., Dufresne, J. L., Fairhead, L., Filiberti, M. A., Friedlingstein, P., Grandpeix, J. Y., Krinner, G., Levan, P., Li, Z. X., and Lott, F.: The LMDZ4 general circulation model: climate performance and sensitivity to parametrized physics with emphasis on tropical convection, Climate Dyn., 27, 787–813, 2006.

Houweling, S., Aben, I., Breon, F. M., Chevallier, F., Deutscher, N., Engelen, R., Gerbig, C., Griffith, D., Hungershoefer, K., Macatangay, R., Marshall, J., Notholt, J., Peters, W., and Serrar, S.: The importance of transport model uncertainties for the estimation of CO2 sources and sinks using satellite measurements, Atmos. Chem. Phys., 10, 9981–9992, 2010.

Huang, X.-Y., Xiao, Q., Barker, D. M., Zhang, X., Michalakes, J., Huang, W., Henderson, T., Bray, J., Chen, Y., Ma, Z., Dudhia, J., Guo, Y., Zhang, X., Won, D.-J., Lin, H.-C., and Kuo, Y.-H.: Four-Dimensional Variational Data Assimilation for WRF: Formulation and Preliminary Results, Mon. Weather Rev., 137, 299–314, 2009.

Jiang, X., Li, Q. B., Liang, M. C., Shia, R. L., Chahine, M. T., Olsen, E. T., Chen, L. L., and Yung, Y. L.: Simulation of upper tropospheric CO2 from chemistry and transport models, Global Biogeochem. Cycles, 22, gB4025, 2008.

Kaminski, T., Rayner, P. J., Heimann, M., and Enting, I. G.: On aggregation errors in atmospheric transport inversions, J. Geophys. Res.-Atmospheres, 106, 4703–4715, 2001.

Kawa, S. R., Erickson, D. J., Pawson, S., and Zhu, Z.: Global CO2 transport simulations using meteorological data from the NASA data assimilation system, J. Geophys. Res.-Atmospheres, 109, d18312, 2004.

Kopacz, M., Jacob, D. J., Henze, D. K., Heald, C. L., Streets, D. G., and Zhang, Q.: Comparison of adjoint and analytical Bayesian inversion methods for constraining Asian sources of carbon monoxide using satellite (MOPITT) measurements of CO columns, J. Geophys. Res.-Atmospheres, 114, d04305, 2009.

Krol, M., Houweling, S., Bregman, B., van den Broek, M., Segers, A., van Velthoven, P., Peters, W., Dentener, F., and Bergamaschi, P.: The two-way nested global chemistry-transport zoom model TM5: algorithm and applications, Atmos. Chem. Phys., 5, 417–432, 2005.

Lanczos, C.: An Iteration Method for the Solution of the Eigenvalue Problem of Linear Differential and Integral Operators, J. Res. Nat. Bur. Stand., 45, 255–282, 1950.

Lauvaux, T., Schuh, A. E., Uliasz, M., Richardson, S., Miles, N., Andrews, A. E., Sweeney, C., Diaz, L. I., Martins, D., Shepson, P. B., and Davis, K. J.: Constraining the CO2 budget of the corn belt: exploring uncertainties from the assumptions in a mesoscale inverse system, Atmos. Chem. Phys., 12, 337–354, 2012.

Lin, J. C., Gerbig, C., Wofsy, S. C., Andrews, A. E., Daube, B. C., Davis, K. J., and Grainger, C. A.: A near-field tool for simulating the upstream influence of atmospheric observations: The Stochastic Time-Inverted Lagrangian Transport (STILT) model, J. Geophys. Res.-Atmospheres, 108, 4493, 2003.

Locatelli, R., Bousquet, P., Chevallier, F., Fortems-Cheney, A., Szopa, S., Saunois, M., Agusti-Panareda, A., Bergmann, D., Bian, H., Cameron-Smith, P., Chipperfield, M. P., Gloor, E., Houweling, S., Kawa, S. R., Krol, M., Patra, P. K., Prinn, R. G., Rigby, M., Saito, R., and Wilson, C.: Impact of transport model errors on the global and regional methane emissions estimated by inverse modelling, Atmos. Chem. Phys., 13, 9917–9937, doi:10.5194/acp-13-9917-2013, 2013.

Mahadevan, P., Wofsy, S. C., Matross, D. M., Xiao, X. M., Dunn, A. L., Lin, J. C., Gerbig, C., Munger, J. W., Chow, V. Y., and Gottlieb, E. W.: A satellite-based biosphere parameterization for net ecosystem CO2 exchange: Vegetation Photosynthesis and Respiration Model (VPRM), Global Biogeochem. Cycles, 22, gB2005, 2008.

Massart, S., Agusti-Panareda, A., Heymann, J., Buchwitz, M., Chevallier, F., Reuter, M., Hilker, M., Burrows, J. P., Deutscher, N. M., Feist, D. G., Hase, F., Sussmann, R., Desmet, F., Dubey, M. K., Griffith, D. W. T., Kivi, R., Petri, C., Schneider, M., and Velazco, V. A.: Ability of

the 4-D-Var analysis of the GOSAT BESD XCO2 retrievals to characterize atmospheric CO2 at large and synoptic scales, Atmos. Chem. Phys., 16, 1653–1671, doi:10.5194/acp-16-1653-2016, 2016.

Meirink, J. F., Bergamaschi, P., Frankenberg, C., d'Amelio, M. T. S., Dlugokencky, E. J., Gatti, L. V., Houweling, S., Miller, J. B., Roeckmann, T., Villani, M. G., and Krol, M. C.: Four-dimensional variational data assimilation for inverse modeling of atmospheric methane emissions: Analysis of SCIAMACHY observations, J. Geophys. Res.-Atmospheres, 113, d17301, 2008.

Menemenlis, D., Campin, J., Heimbach, P., Hill, C., Lee, T., Nguyen, A., Schodlok, M., and Zhang, H.: ECCO2: High Resolution Global Ocean and Sea Ice Data Synthesis, Mercator Ocean Quarterly Newsletter, 31, 13–21, 2008.

Mlawer, E., Taubman, S., Brown, P., Iacono, M., and Clough, S.: Radiative transfer for inhomogeneous atmospheres: RRTM, a validated correlated-k model for the longwave, J. Geophys. Res.-ATMOSPHERES, 102, 16 663–16 682, doi:10.1029/97JD00237, 1997.

Nassar, R., Jones, D. B. A., Suntharalingam, P., Chen, J. M., Andres, R. J., Wecht, K. J., Yantosca, R. M., Kulawik, S. S., Bowman, K. W., Worden, J. R., Machida, T., and Matsueda, H.: Modeling global atmospheric CO2 with improved emission inventories and CO2 production from the oxidation of other carbon species, Geosci. Model Dev., 3, 689–716, 2010.

Nassar, R., Jones, D. B. A., Kulawik, S. S., Worden, J. R., Bowman, K. W., Andres, R. J., Suntharalingam, P., Chen, J. M., Brenninkmeijer, C. A. M., Schuck, T. J., Conway, T. J., and Worthy, D. E.: Inverse modeling of CO2 sources and sinks using satellite observations of CO2 from TES and surface flask measurements, Atmos. Chem. Phys., 11, 6029–6047, 2011.

Nehrkorn, T., Eluszkiewicz, J., Wofsy, S. C., Lin, J. C., Gerbig, C., Longo, M., and Freitas, S.: Coupled weather research and forecasting-stochastic time-inverted lagrangian transport (WRF-STILT) model, Meteorol. Atmos. Phys., 107, 51–64, 2010.

Ott, L., Pawson, S., Collatz, G., Gregg, W. W., Menemenlis, D., Brix, H., Rosseaux, C. S., Bowman, K. W., Liu, J., Eldering, A., Gunson, M. R., and Kawa, S. R.: Assessing the magnitude of CO2 flux uncertainty in atmospheric CO2 records using products from NASA's Carbon Monitoring Flux Pilot Project, J. Geophys. Res.: Atmosphere, 120, doi:10.1002/2014JD022 411, 2015.

Ott, L. E., Bacmeister, J., Pawson, S., Pickering, K., Stenchikov, G., Suarez, M., Huntrieser, H., Loewenstein, M., Lopez, J., and Xueref-Remy, I.: Analysis of Convective Transport and Parameter Sensitivity in a Single Column Version of the Goddard Earth Observation System, Version 5, General Circulation Model, J. Atmos. Sci., 66, 627–646, 2009.

Peters, W., Jacobson, A. R., Sweeney, C., Andrews, A. E., Conway, T. J., Masarie, K., Miller, J. B., Bruhwiler, L. M. P., Petron, G., Hirsch, A. I., Worthy, D. E. J., van der Werf, G. R., Randerson, J. T., Wennberg, P. O., Krol, M. C., and Tans, P. P.: An atmospheric perspective on North American carbon dioxide exchange: CarbonTracker, Proc. Natl. Acad. Sci. U.S.A., 104, 18 925–18 930, 2007.

Pillai, D., Gerbig, C., Marshall, J., Ahmadov, R., Kretschmer, R., Koch, T., and Karstens, U.: High resolution modeling of CO2 over Europe: implications for representation errors of satellite retrievals, Atmos. Chem. Phys., 10, 83–94, 2010.

Pillai, D., Gerbig, C., Kretschmer, R., Beck, V., Karstens, U., Neininger, B., and Heimann, M.: Comparing Lagrangian and Eulerian models for CO2 transport - a step towards Bayesian inverse modeling using WRF/STILT-VPRM, Atmos. Chem. Phys., 12, 8979–8991, 2012.

Pleim, J. E.: A simple, efficient solution of flux-profile relationships in the atmospheric surface layer, J. Appl. Meteorol. and Climatology, 45, 341–347, 2006.

Pleim, J. E.: A combined local and nonlocal closure model for the atmospheric boundary layer. Part I: Model description and testing, J. Appl. Meteorol. and Climatology, 46, 1383–1395, 2007.

Pleim, J. E. and Xiu, A. J.: Development of a land surface model. Part II: Data assimilation, J. Appl. Meteorol., 42, 1811–1822, 2003.

Rabier, F., Jarvinen, H., Klinker, E., Mahfouf, J. F., and Simmons, A.: The ECMWF operational implementation of four-dimensional variational assimilation. I: Experimental results with simplified physics, Quart. J. Roy. Meteor. Soc., 126, 1143–1170, a, 2000.

Geosci. Model Dev. Discuss., doi:10.5194/gmd-2016-289, 2016
Manuscript under review for journal Geosci. Model Dev.
Published: 12 December 2016

Randerson, J. T., Chen, Y., van der Werf, G. R., Rogers, B. M., and Morton, D. C.: Global burned area and biomass burning emissions from small fires, J. Geophys. Res.-BIOGEOSCIENCES, 117, doi:10.1029/2012JG002128, 2012.

Saha, S., Moorthi, S., Wu, X., Wang, J., Nadiga, S., Tripp, P., Behringer, D., Hou, Y.-T., Chuang, H.-Y., Iredell, M., Ek, M., Meng, J., Yang, R., Mendez, M. P., Van Den Dool, H., Zhang, Q., Wang, W., Chen, M., and Becker, E.: The NCEP Climate Forecast System Version 2, J. Climate, 27, 2185–2208, doi:10.1175/JCLI-D-12-00823.1, 2014.

Saito, R., Houweling, S., Patra, P. K., Belikov, D., Lokupitiya, R., Niwa, Y., Chevallier, F., Saeki, T., and Maksyutov, S.: TransCom satellite intercomparison experiment: Construction of a bias corrected atmospheric CO2 climatology, J. Geophys. Res.-Atmospheres, 116, d21120, 2011.

Schuh, A. E., Denning, A. S., Uliasz, M., and Corbin, K. D.: Seeing the forest through the trees: Recovering large-scale carbon flux biases in the midst of small-scale variability, J. Geophys. Res.-Biogeosciences, 114, g03007, 2009.

Stephens, B. B., Gurney, K. R., Tans, P. P., Sweeney, C., Peters, W., Bruhwiler, L., Ciais, P., Ramonet, M., Bousquet, P., Nakazawa, T., Aoki, S., Machida, T., Inoue, G., Vinnichenko, N., Lloyd, J., Jordan, A., Heimann, M., Shibistova, O., Langenfelds, R. L., Steele, L. P., Francey, R. J., and Denning, A. S.: Weak northern and strong tropical land carbon uptake from vertical profiles of atmospheric CO(2), Science, 316, 1732–1735, 2007.

Streets, D. G., Canty, T., Carmichael, G. R., de Foy, B., Dickerson, R. R., Duncan, B. N., Edwards, D. P., Haynes, J. A., Henze, D. K., Houyoux, M. R., Jacobi, D. J., Krotkov, N. A., Lamsal, L. N., Liu, Y., Lu, Z. F., Martini, R. V., Pfister, G. G., Pinder, R. W., Salawitch, R. J., and Wechti, K. J.: Emissions estimation from satellite retrievals: A review of current capability, Atmos. Environ., 77, 1011–1042, 2013.

Thompson, G., Field, P. R., Rasmussen, R. M., and Hall, W. D.: Explicit forecasts of winter precipitation using an improved bulk microphysics scheme. Part II: implementation of a new snow parameterization, Mon. Weather Rev., 136, 5095–5115, 2008.

Tremolet, Y.: Diagnostics of linear and incremental approximations in 4D-Var, Quart. J. Roy. Meteor. Soc., 130, 2233–2251, b, 2004.

Turner, A. J. and Jacob, D. J.: Balancing aggregation and smoothing errors in inverse models, Atmos. Chem. Phys., 15, 7039–7048, 2015.

Uliasz, M.: The Atmospheric Mesoscale Dispersion Modeling System, J. Appl. Meteorol., 32, 139–149, 1993.

Wecht, K. J., Jacob, D. J., Frankenberg, C., Jiang, Z., and Blake, D. R.: Mapping of North American methane emissions with high spatial resolution by inversion of SCIAMACHY satellite data, J. Geophys. Res.-Atmospheres, 119, 7741–7756, 2014.

Wu, L., Bocquet, M., Lauvaux, T., Chevallier, F., Rayner, P., and Davis, K.: Optimal representation of source-sink fluxes for mesoscale carbon dioxide inversion with synthetic data, J. Geophys. Res.-Atmospheres, 116, d21304, 2011.

Zhang, X., Huang, X.-Y., and Pan, N.: Development of the Upgraded Tangent Linear and Adjoint of the Weather Research and Forecasting (WRF) Model, J. Atmos. Oceanic Technol., 30, 1180–1188, 2013.

Geosci. Model Dev. Discuss., doi:10.5194/gmd-2016-289, 2016
Manuscript under review for journal Geosci. Model Dev.
Published: 12 December 2016

Geoscientific Model Development Discussions
Open Access
EGU

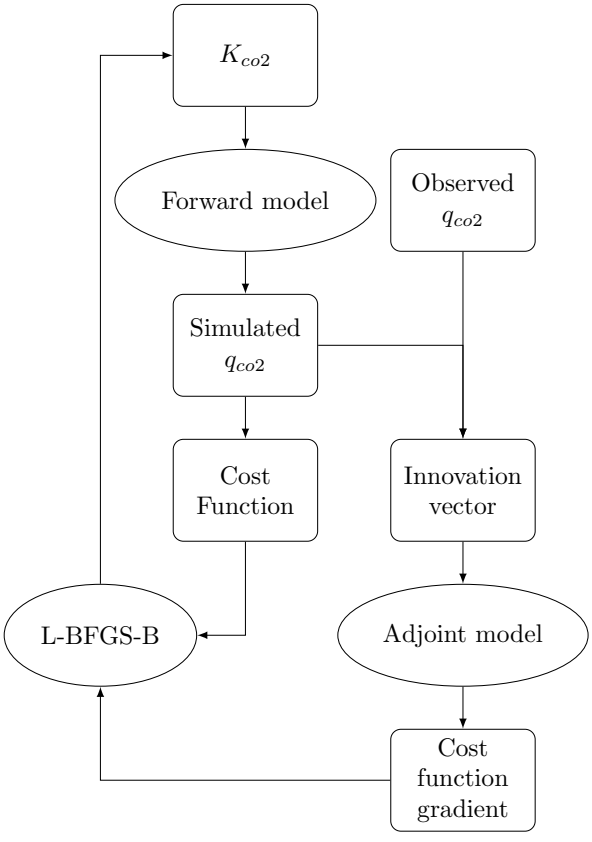

Figure 1. Diagram of L-BFGS-B based optimization implemented for WRF-CO2 4DVar.

Geosci. Model Dev. Discuss., doi:10.5194/gmd-2016-289, 2016
Manuscript under review for journal Geosci. Model Dev.
Published: 12 December 2016

Geoscientific Model Development Discussions

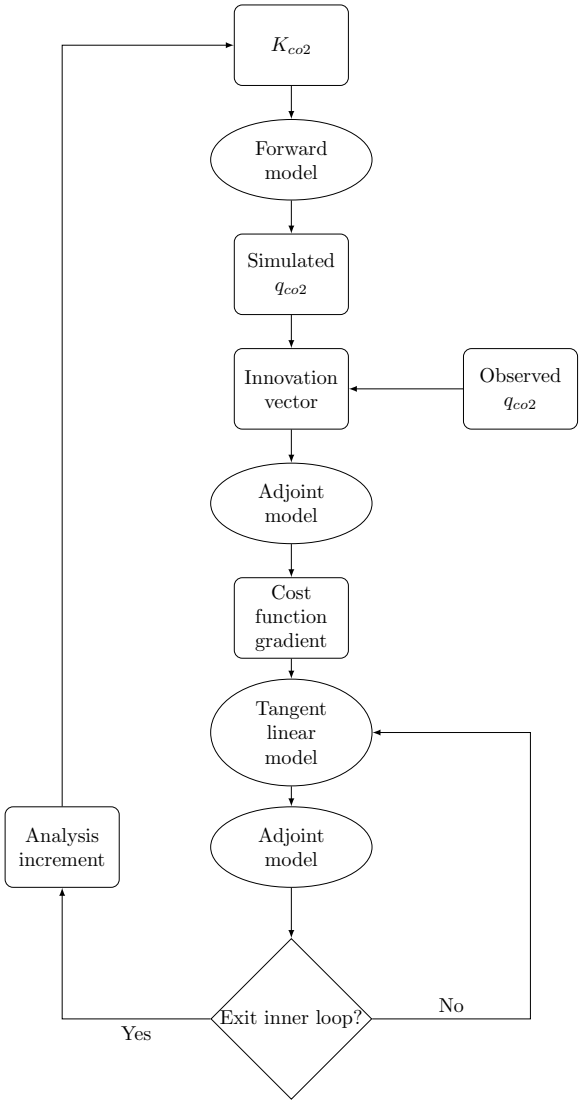

Figure 2. Diagram of Lanczos conjugate gradient (CG) based incremental optimization implemented for WRF-CO2 4DVar

Geosci. Model Dev. Discuss., doi:10.5194/gmd-2016-289, 2016
Manuscript under review for journal Geosci. Model Dev.
Published: 12 December 2016

Geoscientific Model Development Discussions
Open Access
EGU

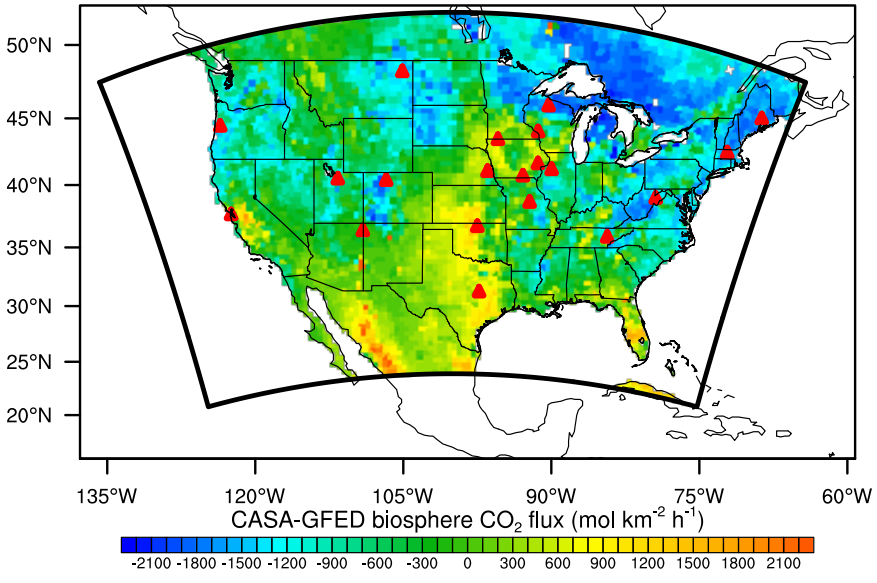

Figure 3. WRF-4DVar simulation domain covering the continental United State with 48 km×48 km grid spacing. The domain is marked by the bold dark outline. Land area is colored by CASA-GFED v4 biosphere CO_2 flux (mol km^{-2} h^{-1}). Locations of 20 CO_2 tower sites are marked by red triangles

Geosci. Model Dev. Discuss., doi:10.5194/gmd-2016-289, 2016
Manuscript under review for journal Geosci. Model Dev.
Published: 12 December 2016

Geoscientific Model Development Discussions
Open Access
EGU

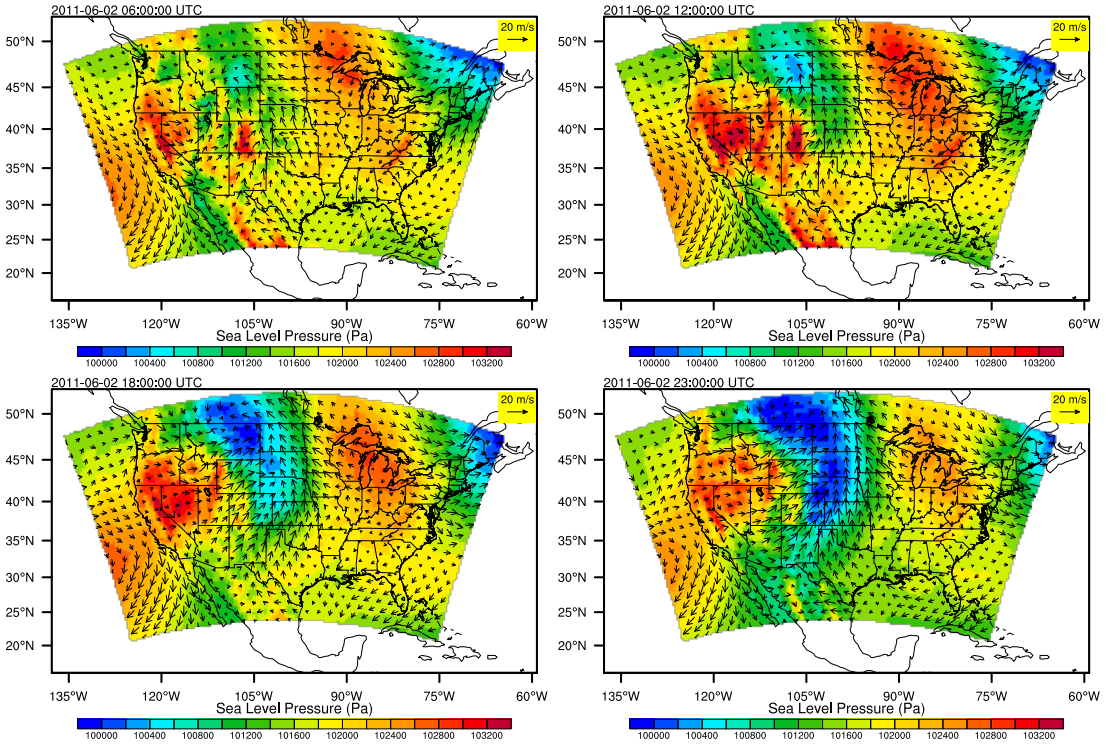

Figure 4. Sea Level Pressure (Pa) and horizontal wind (m s^{-1}) at model's lowest vertical level at 00 UTC, 06 UTC, 12 UTC, and 23 UTC of 2 June 20111.

Geosci. Model Dev. Discuss., doi:10.5194/gmd-2016-289, 2016
Manuscript under review for journal Geosci. Model Dev.
Published: 12 December 2016

Geoscientific Model Development Discussions
Open Access
EGU

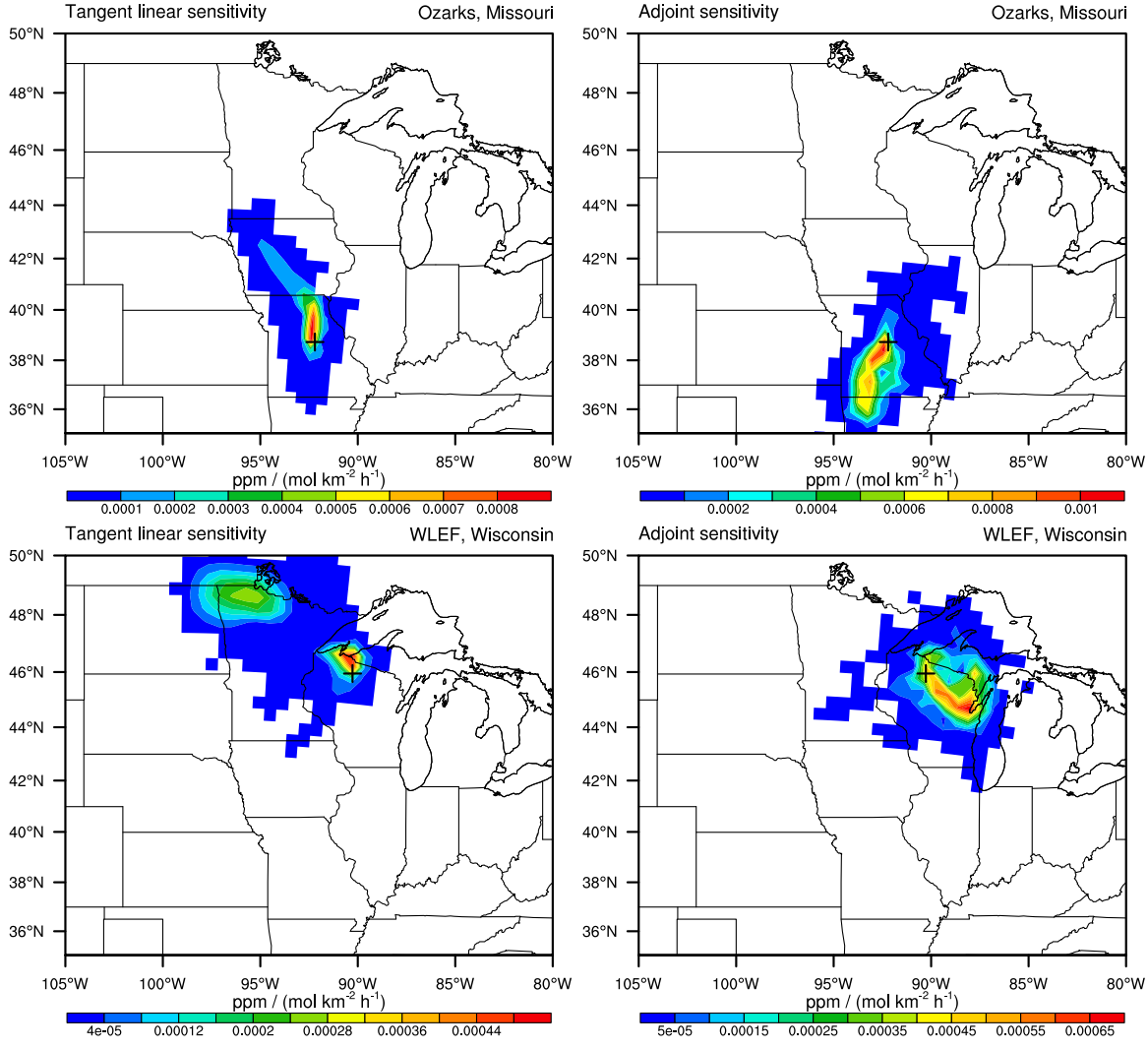

Figure 5. Tangent linear (left) and adjoint sensitivity (right) at Ozarks, Missouri (top) and WLEF, Wisconsin (bottom). These sensitivity values are of unit ppm/(mol km^{-2} h^{-1}) since they are calculated with CO_2 emission set to unity in the tangent linear and adjoint models to exclude the influence of emission magnitude.

Geosci. Model Dev. Discuss., doi:10.5194/gmd-2016-289, 2016
Manuscript under review for journal Geosci. Model Dev.
Published: 12 December 2016

Geoscientific Model Development Discussions
Open Access
EGU

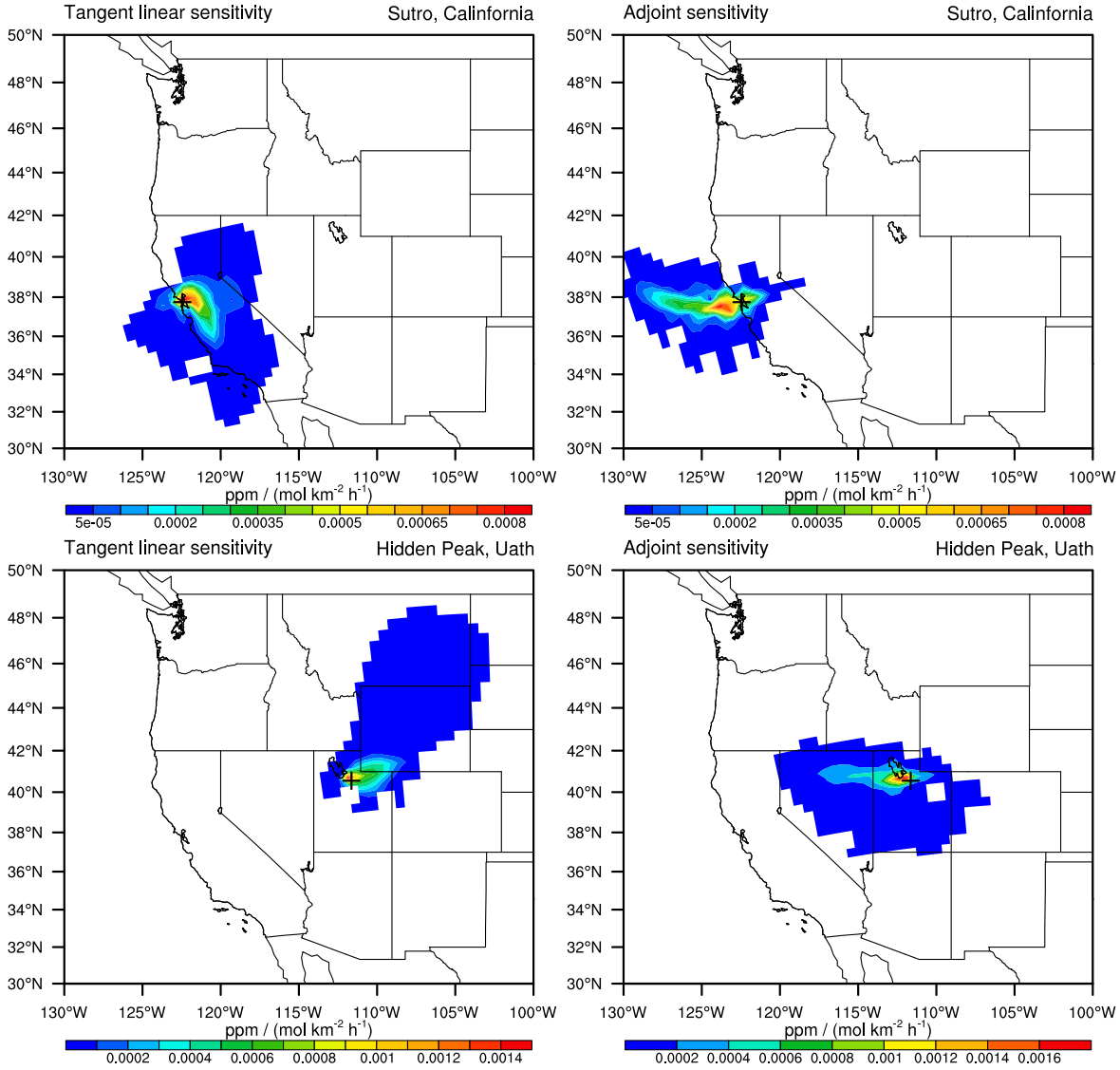

Figure 6. Same as Figure 5 but for Sutro, California (top) and Hidden Peak, Utah (bottom).

Geosci. Model Dev. Discuss., doi:10.5194/gmd-2016-289, 2016
Manuscript under review for journal Geosci. Model Dev.
Published: 12 December 2016

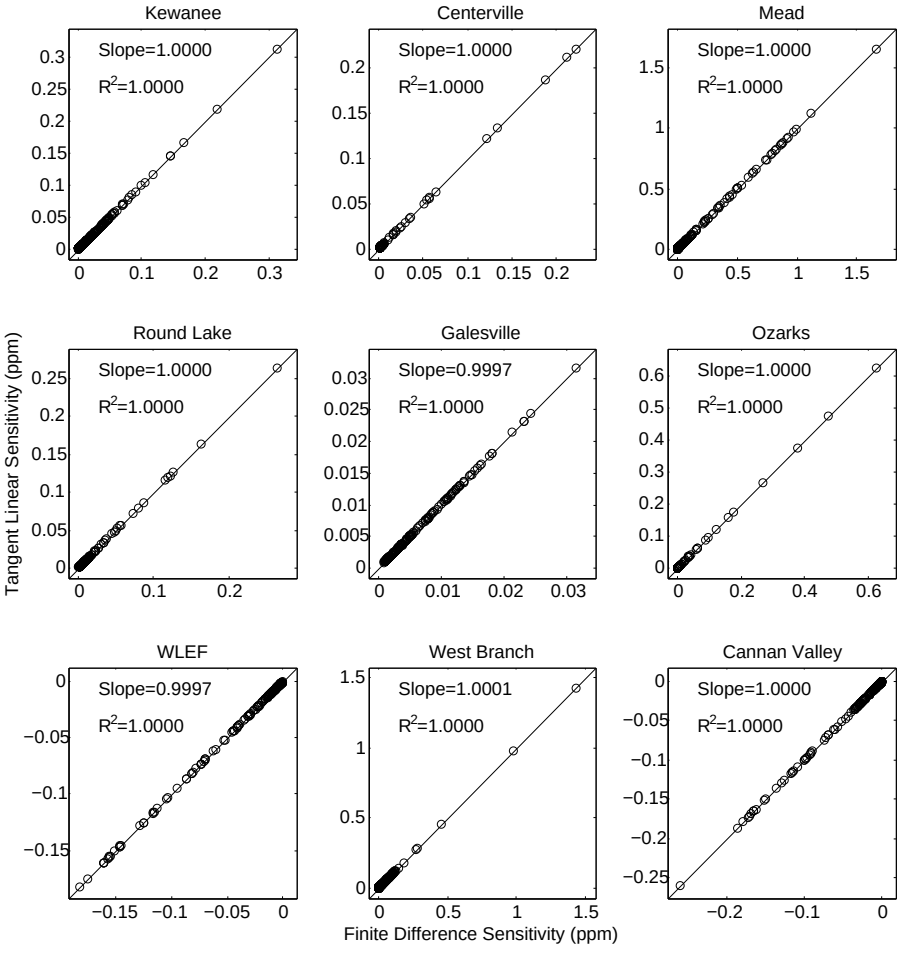

Figure 7. Comparison between $\partial q_{co2}/\partial k_{co2}$ calculated by finite difference (x axis) and tangent linear model (y axis) at nine flux CO_2 tower sites.

Geosci. Model Dev. Discuss., doi:10.5194/gmd-2016-289, 2016
Manuscript under review for journal Geosci. Model Dev.
Published: 12 December 2016

Geoscientific Model Development Discussions
Open Access
EGU

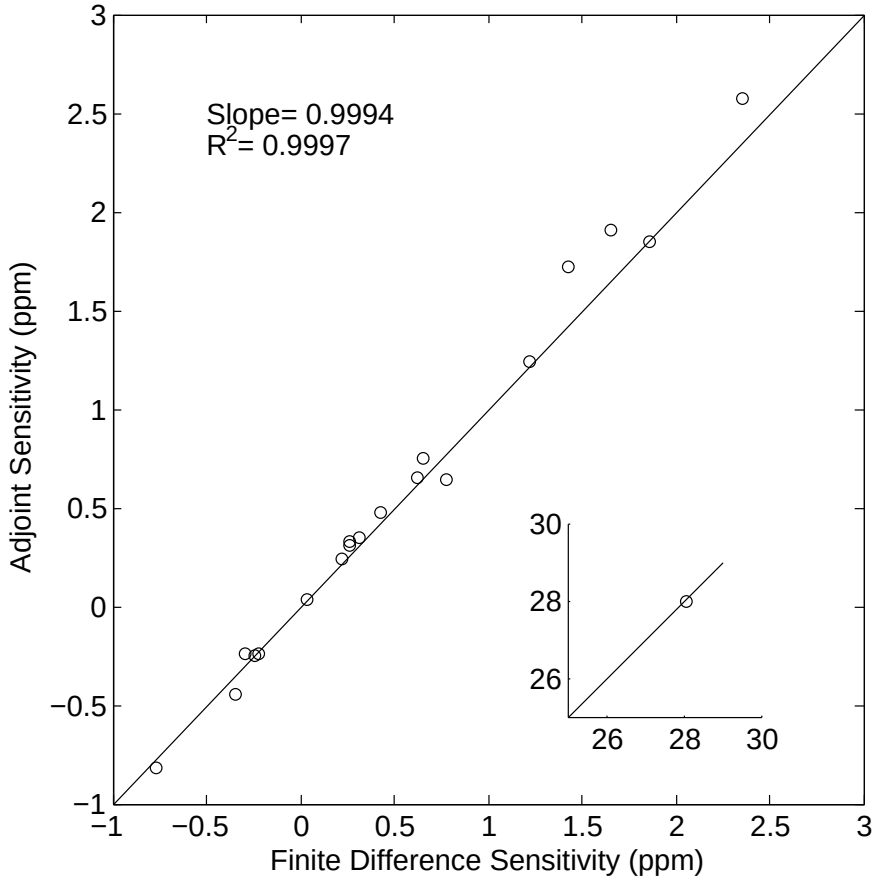

Figure 8. Comparison between $\partial q_{co2}/\partial k_{co2}$ calculated by finite difference (x axis) and adjoint model (y axis) at the model grid of the 20 CO_2 tower sites listed in Table 4. Result at Sutro, California, is shown in an inset due to its much larger magnitude.

Geosci. Model Dev. Discuss., doi:10.5194/gmd-2016-289, 2016
Manuscript under review for journal Geosci. Model Dev.
Published: 12 December 2016

Geoscientific Model Development Discussions

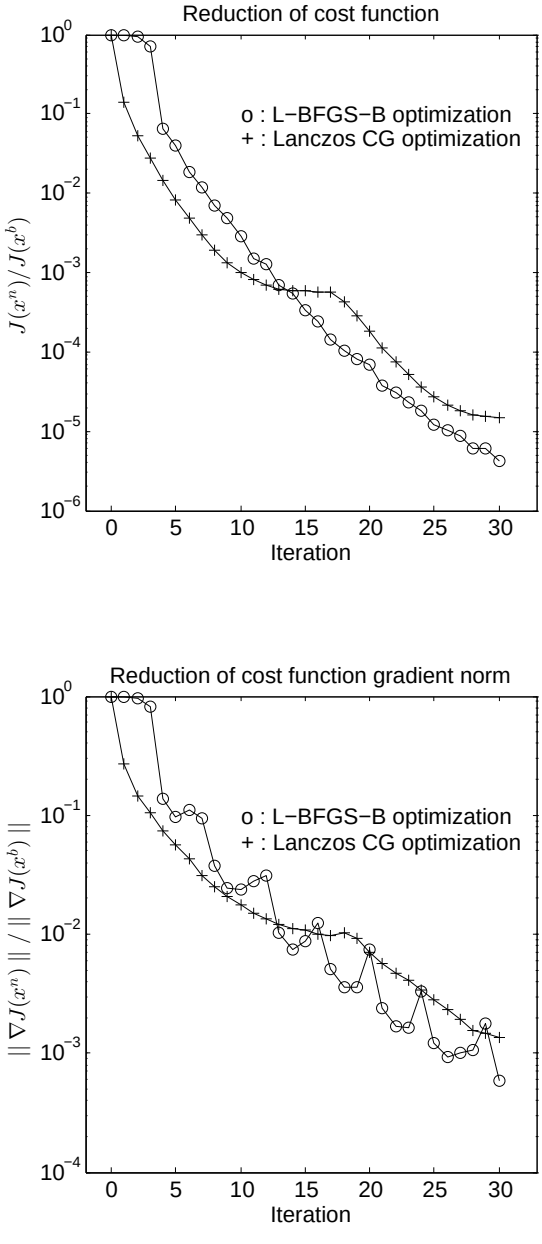

Figure 9. Results of inverse modeling case 1 (prior k_{co2} underestimates the true value by 50%). The top figure shows the reduction of the cost function, represented by $J(x^n)/J(x^b)$, and the bottom figure shows the reduction of the cost function gradient norm, represented by $\|\nabla J(x^n)\| / \left\|\nabla J(x^b)\right\|$.

Geosci. Model Dev. Discuss., doi:10.5194/gmd-2016-289, 2016
Manuscript under review for journal Geosci. Model Dev.
Published: 12 December 2016

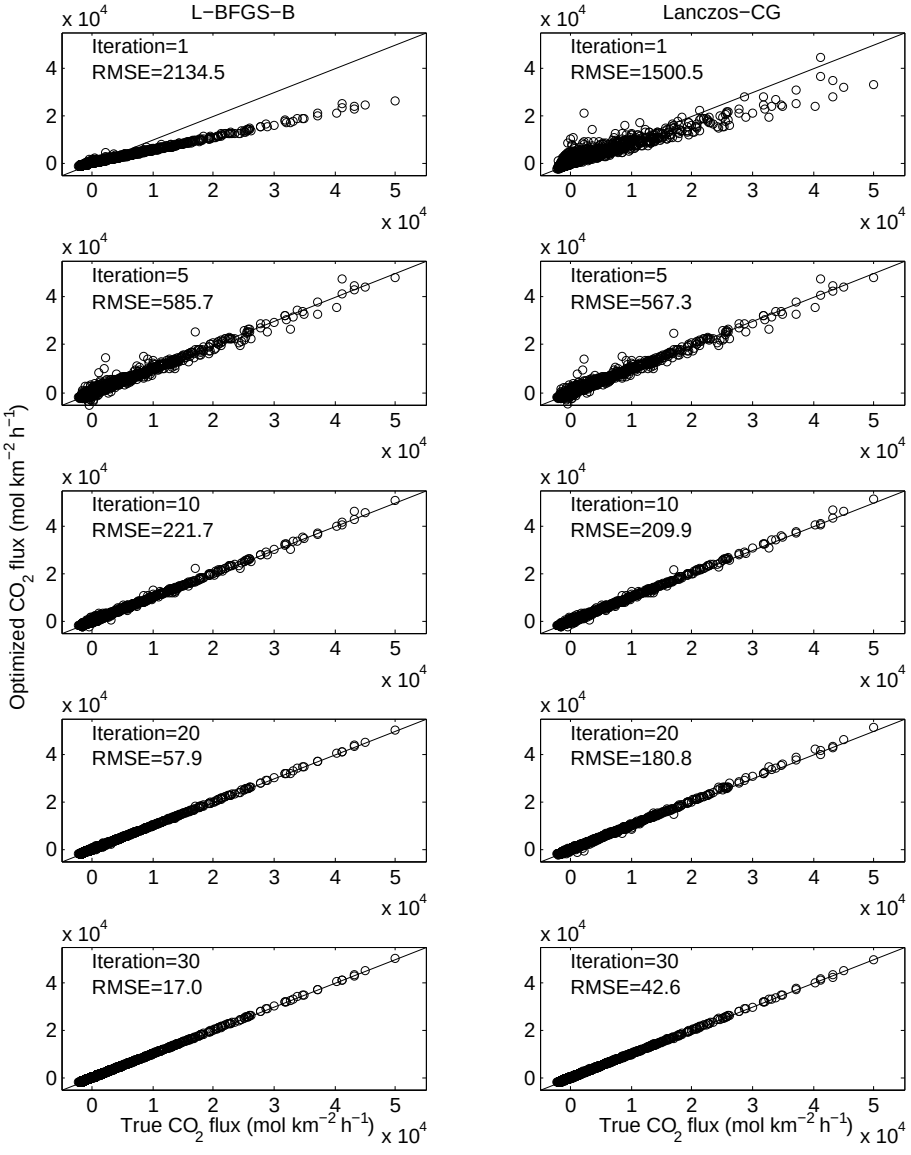

Figure 10. Comparison between the true and optimized CO_2 flux by L-BFGS-B (left column) and Lanczos CG (right column) in inverse modeling case 1 (prior k_{co2} underestimates the true value by 50%). Optimized flux after the 1^{st}, 5^{th}, 10^{th}, 20^{th}, and 30^{th} iterations are shown in the figure.

Geosci. Model Dev. Discuss., doi:10.5194/gmd-2016-289, 2016
Manuscript under review for journal Geosci. Model Dev.
Published: 12 December 2016

Geoscientific Model Development Discussions

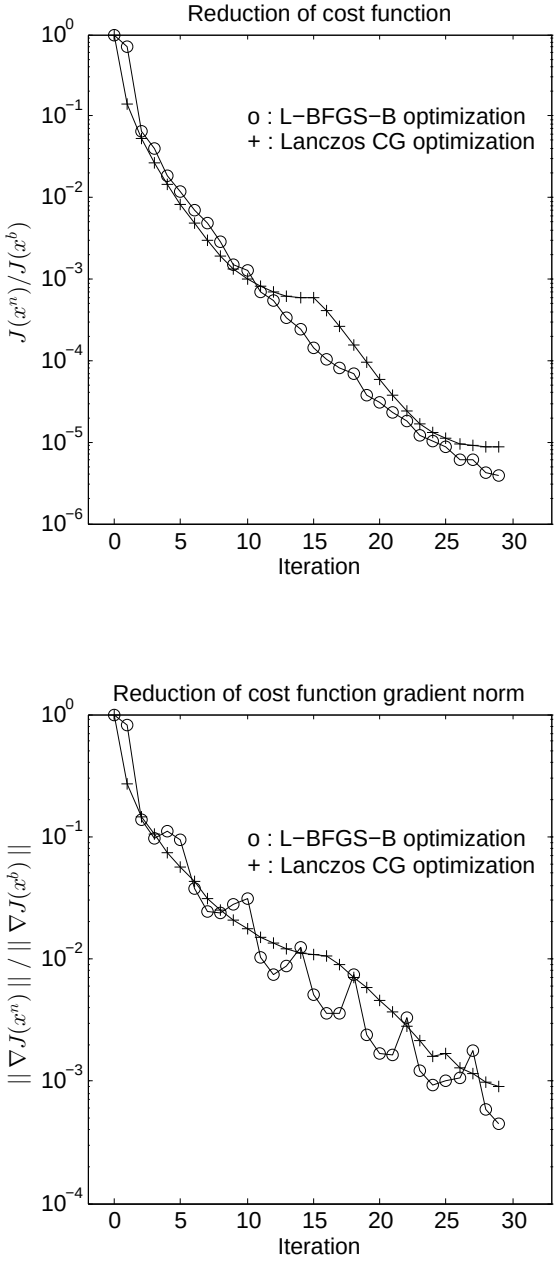

Figure 11. Results of inverse modeling case 2 (prior k_{co2} overestimates the true value by 50%). The top figure shows the reduction of cost function, represented by $J(x^n)/J(x^b)$, and the bottom figure shows the reduction of cost function gradient norm, represented by $\|\nabla J(x^n)\| / \|\nabla J(x^b)\|$.

Geosci. Model Dev. Discuss., doi:10.5194/gmd-2016-289, 2016
Manuscript under review for journal Geosci. Model Dev.
Published: 12 December 2016

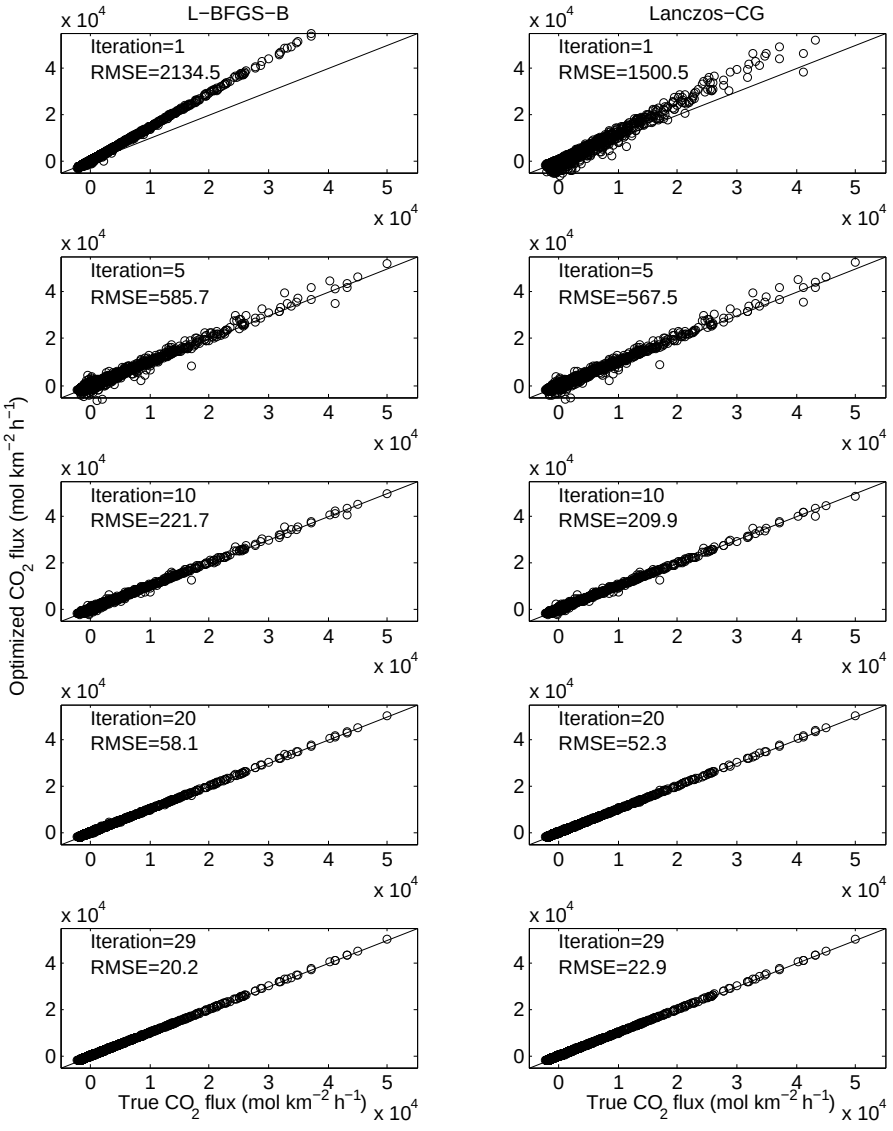

Figure 12. Comparison between the true and optimized CO_2 flux by L-BFGS-B (left column) and Lanczos CG (right column) in inverse modeling case 2 (prior k_{co2} overestimates the true value by 50%). Optimized flux after the 1^{st}, 5^{th}, 10^{th}, 20^{th}, and 29^{th} iterations are shown in the figure.

Geosci. Model Dev. Discuss., doi:10.5194/gmd-2016-289, 2016
Manuscript under review for journal Geosci. Model Dev.
Published: 12 December 2016

Geoscientific Model Development Discussions
Open Access
EGU

Table 1. A list of symbols used in this article

$J(x)$	Cost function
$J_b(x)$	Background cost function
$J_o(x)$	Observation cost function
$\nabla J(x)$	Cost function gradient
$\|\nabla J(x)\|$	Cost function gradient norm
$\nabla^2 J(x)$	Cost function Hessian
$\mathbf{B}$	Background error covariance
$\mathbf{R}$	Observation error covariance
M	WRF-CO2 forward model
$\widetilde{M}$	WRF-CO2 tangent linear model
$\widetilde{M}^T$	WRF-CO2 adjoint model
H	Observation operator
$\widetilde{H}$	Tangent linear observation operator
$\widetilde{H}^T$	Adjoint observation operator
k_{co2}	CO_2 emission scaling factor
q_{co2}	CO_2 mixing ratio (dry air)
g_k_{co2}	Tangent linear variable for CO_2 emission scaling factor
a_k_{co2}	Adjoint variable for CO_2 emission scaling factor
g_q_{co2}	Tangent linear variable for CO_2 mixing ratio (dry air)
a_q_{co2}	Adjoint variable for CO_2 mixing ratio (dry air)
x^b	Prior estimate of CO_2 emission scaling factor
x^n	Analysis of CO_2 emission scaling factor
$\hat{x}$	Analysis increment of CO_2 emission scaling factor
y_k	Observation at the k^{th} assimilation window
d_k	Innovation vector at the k^{th} assimilation window

Geosci. Model Dev. Discuss., doi:10.5194/gmd-2016-289, 2016
Manuscript under review for journal Geosci. Model Dev.
Published: 12 December 2016

Geoscientific Model Development Discussions
Open Access
EGU

Table 2. Summary of variable dependence analysis for developing WRF-CO2 4DVar component models on top of WRFPLUS. In the table, an 'F' means a full physics scheme is used in the forward model, tangent linear model, or the forward sweep of the adjoint model. An 'X' means a process is not needed for CO_2 treatment. A 'Dev' means a process does not exist in WRFPLUS and has been developed for WRF-CO2 4DVar. An 'Add' means a process for CO_2 is simply added using the existing WRFPLUS code for other tracers.

Process	Forward model	Tangent linear model	Adjoint model forward sweep	Adjoint model backward sweep
Radiation	F	F	F	X
Surface	F	F	F	X
Cumulus	F	F	F	X
Microphysics	F	F	F	X
Advection	F	Add	F	Add
Diffusion	F	Add	F	Add
Emission	F	Dev	F	Dev
PBL	F	Dev	F	Dev
Convective transport	F	Dev	F	Dev
Chemistry	X	X	X	X
Photolysis	X	X	X	X
Dry deposition	X	X	X	X
Wet deposition	X	X	X	X

Geosci. Model Dev. Discuss., doi:10.5194/gmd-2016-289, 2016
Manuscript under review for journal Geosci. Model Dev.
Published: 12 December 2016

Geoscientific Model Development Discussions
Open Access
EGU

Table 3. WRF-CO2 4DVar model configuration and emission inventories used in sensitivity and inverse modeling tests.

Longwave radiation	Rapid Radiative Transfer Model (RRTM)
Shortwave radiation	Goddard shortwave
Microphysics	Thompson
Surface layer	Pleim-Xiu
Land surface	Pleim-Xiu
Planetary boundary layer	ACM2 PBL
Cumulus	Grell-Freitas
CO_2 advection	Positive-definite advection
Biosphere CO_2 flux	CASA-GFED v4
Anthropogenic CO_2 emission	EDGAR v4.2
Ocean CO_2 exchange	ECCO2-Darwin

Geosci. Model Dev. Discuss., doi:10.5194/gmd-2016-289, 2016
Manuscript under review for journal Geosci. Model Dev.
Published: 12 December 2016

Geoscientific Model Development Discussions
Open Access
EGU

Table 4. Summary of CO_2 tower sites. Sensitivity $\partial q_{co2}/\partial k_{co2}$ as calculated by WRF-CO2 4DVar's tangent linear and adjoint models is compared against finite difference sensitivity at these sites.

Site Name	Symbol	Latitude	Longitude
Kewanee	RKW	41.28^oN	89.77^oW
Centerville	RCE	40.79^oN	92.88^oW
Mead	RMM	41.14^oN	96.46^oW
Round Lake	RRL	43.53^oN	95.41^oW
Galesville	RGV	44.09^oN	91.34^oW
Ozarks	AMO	38.75^oN	92.2^oW
WLEF	LEF	45.95^oN	9.27^oW
West Branch	WBI	41.73^oN	91.35^oW
Canaan Valley	ACV	39.06^oN	72.94^oW
Chestnut Ridge	ACR	35.93^oN	84.33^oW
Fort Peck	AFP	48.31^oN	105.10^oW
Roof Butte	AFC_RBA	36.46^oN	109.09^oW
Storm Peak Lab	SPL	40.45^oN	106.73^oW
Argle	AMT	45.03^oN	68.68^oW
Harvard Forest	HFM	42.54^oN	72.17^oW
Southern Great Plains	SGP	36.80^oN	97.50^oW
Sutro	STR	37.75^oN	122.45^oW
Hidden Peak	HDP	40.56^oN	111.64^oW
Mary's Peak	ARC_MPK	44.50^oN	123.55^oW
KWKT	KWT	31.31^oN	97.32^oW

Geosci. Model Dev. Discuss., doi:10.5194/gmd-2016-289, 2016
Manuscript under review for journal Geosci. Model Dev.
Published: 12 December 2016

Geoscientific Model Development Discussions
Open Access
EGU

Table 5. Summary of inverse modeling experiment results. The reductions of cost function $J(x)$, cost function gradient norm $\|\nabla J(x)\|$, and RMSE are givne as the ratio to their respective starting values.

Case 1: prior with 50% underestimation (30 iterations)

Reduction in	L-BFGS-B	Lanczos-CG
$J(x)$	0.42×10^{-5}	1.54×10^{-5}
$\|\nabla J(x)\|$	0.6×10^{-3}	1.35×10^{-3}
RMSE	0.72×10^{-2}	1.8×10^{-2}

Case 2: prior with 50% overestimation (29 iterations)

Reduction in	L-BFGS-B	Lanczos-CG
$J(x)$	0.38×10^{-5}	0.87×10^{-5}
$\|\nabla J(x)\|$	0.45×10^{-3}	0.91×10^{-3}
RMSE	0.86×10^{-2}	0.98×10^{-2}